An Investigation of the Effective Climate Sensitivity in GFDL's New Climate Models CM4.0 and SPEAR

MING ZHAO[a]

[a] *Geophysical Fluid Dynamics Laboratory, Princeton, New Jersey*

(Manuscript received 25 April 2021, in final form 22 April 2022)

ABSTRACT: Despite a relatively low climate sensitivity indicated by atmospheric-only simulations with uniform sea surface temperature (SST) warming, GFDL's new climate model CM4.0 participating in CMIP6 and the seasonal-to-decadal prediction system SPEAR, both of which use an identical atmospheric model AM4.0, produce relatively high effective climate sensitivity (EffCS). The substantial increase in CM4.0's EffCS is found to be caused by additional positive forcing associated with the CO_2 fertilization effect on vegetation, enhanced positive feedback due to stronger reduction in Southern Hemisphere (SH) sea ice concentration (SIC), and clouds whose feedback depends on SST warming patterns. Compared to a SPEAR run using a static vegetation model (SPEAR-SV), CM4.0 produces roughly 30% larger EffCS, among which roughly 1/3 of the increase is due to dynamical vegetation with the rest due primarily to changes in SIC. Although cloud feedback does not explain the key feedback differences among CM4.0, SPEAR, and SPEAR-SV, it is the primary cause of the models' increase (less negative) in TOA net feedback during the later period of their quadrupling CO_2 simulations due to changes in their SST warming patterns. Moreover, CM4.0's SST warming pattern and its effects on cloud feedback appear to be the leading cause of CM4.0's EffCS increase compared to the earlier generation GFDL model ESM2M, which produces one of the lowest EffCS values among CMIP5 models. In comparison, CM4.0's enhanced reduction in SH SICs plays a slightly less important role in its increase in EffCS compared to ESM2M.

KEYWORDS: Atmosphere-ocean interaction; Vegetation-atmosphere interactions; Climate change; Climate sensitivity; Cloud radiative effects; Feedback; Climate models; Clouds; Coupled models; Ecosystem effects

1. Introduction

Equilibrium climate sensitivity (ECS) of the Earth system is an idealized metric defined as the global mean surface air temperature (SAT) change that results from a doubling of atmospheric CO_2 concentration over the preindustrial level after the climate system reaches equilibrium. Model estimates of ECS, which is often characterized as effective climate sensitivity (EffCS), have varied substantially since the first IPCC assessment report (e.g., 1.5–4.5 K) and their uncertainty range has proven difficult to reduce (e.g., Meehl et al. 2020). A recent assessment has reduced the EffCS uncertainty range using multiple lines of evidence including process understanding, the historical climate record, and the paleoclimate record with a Bayesian approach (Sherwood et al. 2020). By bringing in some observational constraints, Myers et al. (2021) also showed an ability to reduce the EffCS uncertainty range. Despite these recent efforts, it remains imperative to understand and narrow down modeled EffCS uncertainty since a model's EffCS is highly correlated with its transient climate response (TCR) (e.g., Meehl et al. 2020) and future climate projections depend crucially on TCR and EffCS as essential model characteristic (e.g., Grose et al. 2018).

The large range of modeled EffCS has long been attributed to intermodel differences in cloud feedbacks (e.g., Cess et al. 1996; Bony et al. 2004; Bony and Dufresne 2005; Webb et al. 2006, 2013; Zhao 2014; Zhao et al. 2016; Satoh et al. 2018). During the past decade, there have been numerous proposed emergent constraints on EffCS using Coupled Model Intercomparison Project (CMIP) phase 3 and 5 (CMIP3/CMIP5) model outputs in conjunction with observations (e.g., Brient and Schneider 2016; Cox et al. 2018; Sherwood et al. 2014; Klein and Hall 2015). However, a recent study by Schlund et al. (2020) evaluated 11 published emergent constraints on EffCS and found that nearly all of them failed when used with CMIP6 (Eyring et al. 2016) models with a large decrease in correlation coefficients between the models' EffCS and proposed parameters/indices. It is worth noting that, except for Cox et al. (2018), which is based on temperature variability, all of the emergent constraints analyzed in Schlund et al. (2020) are directly or indirectly based on cloud processes. While the causes of this failure are still unclear, this seems to indicate that cloud processes alone might not be sufficient in constraining modeled EffCS values, and processes other than clouds might also contribute substantially to CMIP6 models' uncertainties in EffCS.

The development of GFDL's new atmospheric model AM4.0 (Zhao et al. 2018a,b) paid special attention to the model's cloud feedbacks and climate sensitivity by frequently conducting a Cess-style experiment and assessing the cloud feedback and Cess climate sensitivity (e.g., Cess et al. 1990). The Cess experiment is an idealized global warming simulation with a uniform 2-K increase in sea surface temperatures (SST) while keeping everything else identical to the control

---

Supplemental information related to this paper is available at the Journals Online website: https://doi.org/10.1175/JCLI-D-21-0327.s1.

Corresponding author: Ming Zhao, ming.zhao@noaa.gov

DOI: 10.1175/JCLI-D-21-0327.1

simulation. The Cess feedback can be computed as the global top-of-atmosphere (TOA) radiation anomaly divided by the global mean SAT anomaly. The Cess EffCS can then be estimated as the effective radiative forcing (ERF) of a doubling of atmospheric CO_2 concentration divided by this Cess feedback value. Cess experiments have been widely used among the climate modeling and analysis communities especially for model intercomparison projects (e.g., Cess et al. 1996; Wyant et al. 2006; Medeiros et al. 2008; Zhao 2014; Ringer et al. 2014; Webb et al. 2015; Zhao et al. 2016).

While we do not expect the Cess EffCS to be equivalent to a coupled model's EffCS, we do anticipate it to be a good predictor of the coupled EffCS in the sense that it should be reasonably well correlated with the EffCS in its coupled model. However, to our surprise, we found that while AM4.0 produces a Cess EffCS ($2.56\ \mathrm{K} = 4\ \mathrm{W\ m^{-2}}/1.56\ \mathrm{W\ m^{-2}\ K^{-1}}$, assuming $\mathrm{ERF}_{2\mathrm{xCO}_2} = 4\ \mathrm{W\ m^{-2}}$) very similar to the earlier GFDL model AM2 (Anderson et al. 2004) ($2.48\ \mathrm{K} = 4\ \mathrm{W\ m^{-2}}/1.61\ \mathrm{W\ m^{-2}\ K^{-1}}$, assuming $\mathrm{ERF}_{2\mathrm{xCO}_2} = 4\ \mathrm{W\ m^{-2}}$), CM4.0, the GFDL's new climate model that uses AM4.0 and has participated in CMIP6 (Held et al. 2019), produces an EffCS of ~5 K (Winton et al. 2019), which is much higher than that (~2.9 K; see Table 3 and Fig. 1) of GFDL's ESM2M (Dunne et al. 2012), which used AM2 and participated in CMIP5. These EffCS values of CM4.0 and ESM2M (see Table 3) were estimated using the same Gregory method (Gregory et al. 2004; Andrews et al. 2015) with two separate linear regressions for the earlier (first 50 years) and later period (last 100 years) of an abrupt $4xCO_2$ simulation (total 150 years) to account for the effect of time-varying feedback (e.g., Winton et al. 2019). Note that the exact EffCS numbers may differ among different studies due to differences in method of estimation. For example, the EffCS of CM4.0 and ESM2M are documented as 3.9 and 2.4 K, respectively, in Meehl et al. (2020) when compared with other models using a single linear regression of the entire 150-yr abrupt $4xCO_2$ simulation (Gregory et al. 2004).

In this study, we attempt to investigate the causes of EffCS increase in CM4.0 in comparison to GFDL's Seamless System for Prediction and Earth System Research [SPEAR; Delworth et al. (2020)], a SPEAR run using a static vegetation model, as well as the earlier generation GFDL ESM2M, which uses AM2 and produces one of the lowest EffCS values among CMIP5 models (Meehl et al. 2020). During this process, we quantify how the relatively strong negative feedback seen in AM4.0's Cess simulation (similar to AM2) is weakened as AM4.0 is coupled to the ocean and sea ice model OM4 (Adcroft et al. 2019) and the dynamical vegetation model (Shevliakova et al. 2009) used in CM4.0. CM4.0 and SPEAR use an identical atmospheric model (AM4.0), which is coupled to the same ocean and sea ice model OM4 (Adcroft et al. 2019) with different horizontal resolutions (CM4.0 uses 0.25° OM4 while SPEAR uses 1° OM4). Because of their difference in ocean model resolution, they also differ in the oceanic physics parameterizations, which have been documented in Delworth et al. (2020). The similarity between CM4.0 and SPEAR would make it straightforward to attribute some of the CM4.0's increase in EffCS (i.e., from 4.2 K in SPEAR to 5 K in CM4.0) to their differences in the ocean and sea ice model. An additional experiment running SPEAR with a static vegetation model would help to quantify the effect of dynamical vegetation in CM4.0 and SPEAR. Moreover, running AM4.0 with prescribed SST, sea ice concentration (SIC), and

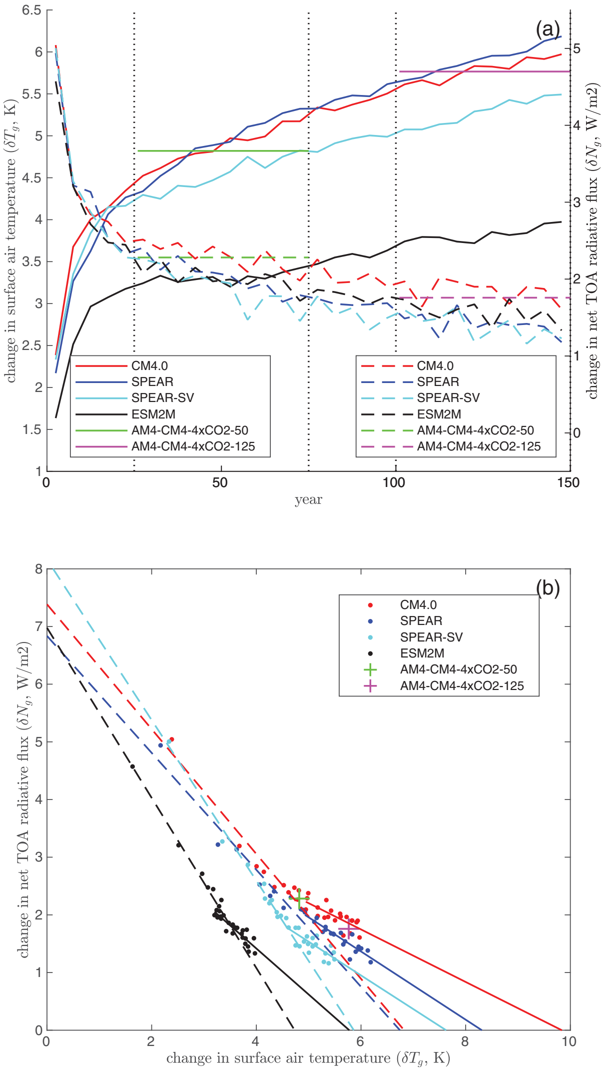

FIG. 1. (a) Left ordinate/legend: Time evolution of the change in global mean surface air temperature (δT_g) in response to an abrupt 4 times increase of atmospheric CO_2 concentration from CM4.0, SPEAR, SPEAR-SV, and ESM2M. Each point represents a 5-yr average. Right ordinate/legend: As in the left ordinate/legend, but for global mean TOA net radiative flux (δN_g, downward positive). The horizontal lines denote δT_g and δN_g from two uncoupled AM4.0 simulations with prescribed SSTs, SICs, static vegetation, and CO_2 concentration derived from two periods [centered at year 50 (Y50) and year 125 (Y125)] of CM4.0's $4xCO_2$ simulation (see Table 1 for a description of the simulations). (b) As in (a), but for scatterplots of δN_g vs δT_g. The dashed and solid lines are respectively a linear regression based on the first 50-yr and the last 100-yr simulation of each model. The intercepts of the solid lines with the x axis divided by 2 provide an estimate of the effective climate sensitivity for each model. The two cross symbols indicate δN_g vs δT_g from the two uncoupled AM4.0 simulations shown in (a).

vegetation anomalies derived from coupled simulations would help to study their effects in isolation. Recent studies suggest that differences in SST warming patterns can also substantially modify modeled climate feedback strength and therefore may be a significant source of uncertainty in modeled EffCS (e.g., Andrews et al. 2015; Gregory and Andrews 2016; Zhou et al. 2017; Andrews and Webb 2018; Andrews et al. 2018; Silvers et al. 2018; Paynter and Frölicher 2015; Winton et al. 2010; Dong et al. 2019; Gregory et al. 2020). Thus, running AM4.0 forced by SST warming patterns derived from CM4.0 and ESM2M would help quantify the SST pattern effect on their EffCS difference. Below section 2 describes the models and simulations, section 3 presents the results, and section 4 provides a summary.

2. The models and simulations

Here we focus on an investigation of GFDL new climate models CM4.0 (Held et al. 2019) and SPEAR (Delworth et al. 2020). Both models use an identical atmosphere and land model (i.e., AM4.0/LM4.0) described in Zhao et al. (2018a,b) and a dynamical vegetation model that was not used in Zhao et al. (2018a,b). However, CM4.0 and SPEAR differ in their configuration of the Modular Ocean Model version 6 (MOM6) ocean model (Adcroft et al. 2019). In particular, CM4.0 uses a 0.25° horizontal resolution MOM6 while SPEAR uses a 1° MOM6. As a result, they also differ in oceanic physics parameterizations. For example, SPEAR uses a mesoscale eddy parameterization while CM4.0 does not. While both SPEAR and CM4.0 use the same submesoscale eddy parameterization, they choose different parameter coefficients. Moreover, an extra horizontal viscosity poleward of 50° in each hemisphere is applied in SPEAR to empirically improve some aspects of the ocean simulation for a coarser-resolution ocean model. But this is not applied in CM4.0. We refer to Held et al. (2019) and Delworth et al. (2020) for the details of CM4.0 and SPEAR. Finally, it is worth noting that compared to CM4.0, SPEAR is a much faster model due to its fourfold reduction in the ocean model's resolution and that most (~80%) of the CM4.0 computational cost is used for the ocean model. Thus, SPEAR is a much cheaper model for exploring the EffCS of a coupled AM4.0 and its potential variant.

For both CM4.0 and SPEAR, the simulations we explore here include a control simulation with the models forced by preindustrial concentrations of radiative gases, aerosol emissions, solar irradiance, and background volcanic forcing following CMIP6 specifications (referred to as pi-Control below) and an idealized warming simulation which is identical to pi-Control except with an abrupt quadrupling of the atmospheric CO_2 concentration from its pi-Control value (referred to as $4xCO_2$ below). As noted before, CM4.0 and SPEAR use the same dynamical vegetation model, which allows vegetation to evolve with environment conditions. To quantify the role of dynamical vegetation in the models' EffCS, we have conducted a pair of SPEAR simulations in which the vegetation is kept fixed at the present-day condition (i.e., we use a static instead of a dynamic vegetation model, referred to as SPEAR-SV below). While this study focuses on the latest GFDL climate models, we also include some results from the $4xCO_2$ and pi-Control of the earlier coupled model ESM2M when it is appropriate and the output are available.

To separate the effects of SST warming and changes in SICs and vegetation on CM4.0's feedback and EffCS, we have conducted a series of uncoupled AM4.0 simulations (each simulation is integrated for 21 years with the last 20-yr output used for analysis) with the model forced by climatological SSTs, SICs, and vegetation derived from CM4.0's pi-Control and two periods of its corresponding $4xCO_2$ simulation. Note that we did not take into account any changes in sea ice thickness. All uncoupled AM4.0 simulations used prescribed 2-m sea ice thickness. The prescribed vegetation data include variables such as vegetation type, the biomass of leaves, fine roots, sapwood, heartwood, and leaf status. These static characteristics capture the seasonal cycle of vegetation, which can, in turn, affect land characteristics such as roughness and albedo.

The preindustrial climatology of CM4.0 is computed from a 100-yr average of CM4.0's pi-Control and used for AM4-CM4-C (C denotes pi-Control). The first period of the $4xCO_2$ warmed climatology is obtained by taking the average of SSTs and SICs from years 26–75 (Y50) of CM4.0's $4xCO_2$ simulation. This is referred to as AM4-CM4-$4xCO_2$-50. The vegetation data use the output from year 50 of CM4.0's $4xCO_2$ simulation. The second period is obtained by taking the average of SSTs and SICs from years 101–150 (Y125) of CM4.0's $4xCO_2$ simulation and it is denoted as AM4-CM4-$4xCO_2$-125. Note the total length of the coupled $4xCO_2$ simulation spans 150 years. Compared to AM4-CM4-C, AM4-CM4-$4xCO_2$-50 (or AM4-CM4-$4xCO_2$-125) contains anomalous perturbations of four fields (SSTs, SICs, vegetation, and CO_2 concentration). Thus, AM4-CM4-C and AM4-CM4-$4xCO_2$-50 (or AM4-CM4-$4xCO_2$-125) can be used to verify the extent to which the uncoupled AM4.0 is able to reproduce CM4.0 simulated response to a quadrupling of CO_2 concentration.

To assess the modeled climate feedback, we have also conducted a simulation identical to AM4-CM4-$4xCO_2$-50 (AM4-CM4-$4xCO_2$-125) except using the CO_2 concentration from pi-Control; this run is referred to as AM4-CM4-50 (AM4-CM4-125). The difference between AM4-CM4-C and AM4-CM4-50 (AM4-CM4-125) can be used to assess the total climate feedback due to SST, SIC, and vegetation anomalies in CM4.0's $4xCO_2$ simulation. In addition, we have carried out three AM4.0 simulations (i.e., AM4-CM4-SST-50, AM4-CM4-SIC-50, AM4-CM4-VEG-50) similar to AM4-CM4-50 except with the SST, SIC, and vegetation anomalies, respectively, added to AM4-CM4-C one at a time to obtain the contribution to total feedback from each individual component. Similarly, we also conducted three AM4.0 simulations (i.e., AM4-CM4-SST-125, AM4-CM4-SIC-125, AM4-CM4-VEG-125) similar to AM4-CM4-125 except with the SST, SIC, and vegetation anomalies, respectively, added to AM4-CM4-C.

In coupled simulations with dynamical vegetation, the vegetation response to CO_2 increase may result from two different sources. The first is a direct response due to CO_2 fertilization and/or CO_2-induced changes in evapotranspiration (stomatal contractions) which are independent of a change in temperature.

TABLE 1. A list of the coupled model simulations and the uncoupled AM4.0 experiments forced by CM4.0's SSTs, sea ice concentrations, and vegetation including a short description of each simulation.

Model	Simulation	Description
CM4.0	pi-Control	CM4.0 forced by preindustrial radiative gases and aerosol emissions
	4xCO_2	As in pi-Control, except with 4 times increase of CO_2 concentration
SPEAR	pi-Control	SPEAR forced by preindustrial radiative gases and aerosol emissions
	4xCO_2	As in pi-Control, except with 4 times increase of CO_2 concentration
SPEAR-SV	pi-Control	SPEAR-SV forced by preindustrial radiative gases and aerosol emissions
	4xCO_2	As in pi-Control, except with 4 times increase of CO_2 concentration
ESM2M	pi-Control	ESM2M forced by preindustrial radiative gases and aerosol emissions
	4xCO_2	As in pi-Control, except with 4 times increase of CO_2 concentration
AM4.0	AM4-CM4-C	AM4.0 forced by the climatological SSTs, SICs, static vegetation, CO_2, and other radiative gases and aerosol emissions derived from CM4.0's pi-Control
AM4.0	AM4-CM4-4xCO_2-50	As in AM4-CM4-C, except adding CO_2, SST, SIC, and vegetation differences averaged from years 26–75 of the 4xCO_2 and pi-Control of CM4.0
AM4.0	AM4-CM4-50	As in AM4-CM4-C, except adding SST, SIC, and vegetation differences/anomalies averaged from years 26–75 of the 4xCO_2 and pi-Control of CM4.0
AM4.0	AM4-CM4-SST-50	As in AM4-CM4-C, except only adding SST anomalies averaged from years 26–75 of the 4xCO_2 and pi-Control of CM4.0
AM4.0	AM4-CM4-SIC-50	As in AM4-CM4-C, except only adding SIC anomalies averaged from years 26–75 of the 4xCO_2 and pi-Control of CM4.0
AM4.0	AM4-CM4-VEG-50	As in AM4-CM4-C, except only adding vegetation anomalies from year 50 of the 4xCO_2 and pi-Control of CM4.0
AM4.0	AM4-CM4-4xCO_2-125	As in AM4-CM4-C, except adding CO_2, SST, SIC, and vegetation differences averaged from years 101–150 of the 4xCO_2 and pi-Control of CM4.0
AM4.0	AM4-CM4-125	As in AM4-CM4-C, except adding SST, SIC, and vegetation difference/anomalies averaged from years 101–150 of the 4xCO_2 and pi-Control of CM4.0
AM4.0	AM4-CM4-SST-125	As in AM4-CM4-C, except only adding SST anomalies averaged from years 101–150 of the 4xCO_2 and pi-Control of CM4.0
AM4.0	AM4-CM4-SIC-125	As in AM4-CM4-C, except only adding SIC anomalies averaged from years 101–150 of the 4xCO_2 and pi-Control of CM4.0
AM4.0	AM4-CM4-VEG-125	As in AM4-CM4-C, except only adding vegetation anomalies from year 125 of the 4xCO_2 and pi-Control of CM4.0
AM4.0	AM4-CM4-C-DVEG	As in AM4-CM4-C, except with dynamic vegetation model turned on
AM4.0	AM4-CM4-C-DVEG-4xCO_2	As in AM4-CM4-C-DVEG, except with the dynamic vegetation model fed with 4 times the value of CO_2 concentration from its pi-Control

The second is a temperature-mediated change, which may involve changes in a large-scale meteorology environment. To quantify the direct response of vegetation and its impact on TOA radiative forcing, we have conducted a pair of uncoupled AM4.0 simulations identical to AM4-CM4-C except with the dynamic vegetation model turned on and fed with two different values of CO_2 concentration (i.e., pi-Control value for AM4-CM4-C-DVEG and 4 times the pi-Control value for AM4-CM4-C-DVEG-4xCO2). Note that the atmospheric radiative transfer code in both simulations sees only the pi-Control value of the atmospheric CO_2 concentration. Because it takes about 20 years for vegetation to equilibrate with the abrupt increase in CO_2 in AM4.0, we integrated both simulations for 51 years with the last 50 years used for analysis. Table 1 provides a list of the simulations described above including their short descriptions.

Finally, to explore the effects of SST warming patterns on climate feedbacks in AM4.0/CM4.0, we have conducted eight AM4.0 simulations that are identical to AM4-CM4-C except with prescribed SST warming patterns. The global area-weighted mean SST warming anomaly is 2 K for all cases. The warming patterns include a uniform 2-K SST increase (AM4-uniform2K) and the SST warming patterns derived from years 26–75 (AM4-CM4pattern2K-50) and years 101–150 (AM4-CM4pattern2K-125) of CM4.0's 4xCO_2 as compared to its pi-Control. Because the AM4-CM4pattern2K-125 SST warming pattern is dominated by the earlier period when compared to its pi-Control, we have also included a simulation (AM4-CM4pattern2K-125minus50) with the warming pattern derived from the two periods (i.e., years 26–75 vs years 101–150). In each case, SST warming anomalies are computed by taking the corresponding difference, dividing by their global ocean area-weighted mean difference, and then multiplying by 2 K. To compare the effects of CM4.0's warming patterns with those from GFDL's earlier generation ESM2M model, we have conducted three additional simulations (AM4-ESM2Mpattern2K-50, AM4-ESM2Mpattern2K-125, and AM4-ESM2Mpattern2K-125minus50) using SST warming patterns similarly derived as CM4.0 except from ESM2M's 4xCO_2 and pi-Control simulations. Furthermore, to identify key features of SST warming patterns that are important to the feedback differences between CM4.0 and ESM2M, we have carried out a simulation (AM4-CM4pattern2K-125-modified) that is identical to AM4-CM4pattern2K-125 except with its zonal-mean SST warming anomalies replaced by those from

TABLE 2. A list of uncoupled AM4.0 simulations identical to AM4-CM4-C (in Table 1) except with prescribed SST warming patterns/anomalies. The SST warming anomalies are computed by taking the difference between CM4.0's or ESM2M's coupled 4xCO_2 and its corresponding pi-Control simulation, dividing by their global ocean area-weighted mean difference, and then multiplying by two so that the global mean SST warming is 2 K for each simulation.

Model	Simulation	Description of SST anomalies
AM4.0	AM4-uniform2K	2 K uniformly (Cess simulation)
AM4.0	AM4-CM4pattern2K-50	SST anomalies averaged from years 26–75 of CM4.0's 4xCO_2 (cf. to its pi-Control)
AM4.0	AM4-CM4pattern2K-125	SST anomalies averaged from years 101–150 of CM4.0's 4xCO_2 (cf. to its pi-Control)
AM4.0	AM4-CM4pattern2K-125minus50	Difference in SST anomalies between years 101–150 and years 26–75 of CM4.0's 4xCO_2
AM4.0	AM4-ESM2Mpattern2K-50	SST anomalies averaged from years 26–75 of ESM2M's 4xCO_2 (cf. to its pi-Control)
AM4.0	AM4-ESM2Mpattern2K-125	SST anomalies averaged from years 101–150 of ESM2M's 4xCO_2 (cf. to its pi-Control)
AM4.0	AM4-ESM2Mpattern2K-125minus50	Difference in SST anomalies between years 101–150 and years 26–75 of ESM2M's 4xCO_2
AM4.0	AM4-CM4pattern2K-125-modified	As in AM4-CM4pattern2K-125, except with its zonal mean SST anomalies replaced by those from AM4-ESM2Mpattern2K-125

AM4-ESM2Mpattern2K-125 (i.e., subtracting its own zonal-mean SST anomalies and adding the zonal-mean SST anomalies from AM4-ESM2Mpattern2K-125). Table 2 provides a description of the eight simulations for exploring the effects of SST warming patterns. Below we present the results and explain the causes of CM4.0's increase in EffCS using the various coupled model simulations and the uncoupled AM4.0 simulations with prescribed SSTs, SICs, vegetation, and SST warming patterns.

3. Results

a. Coupled model simulations

We first show in Fig. 1a the time evolution of the change in global mean SAT (δT_g) and TOA net radiative flux (δN_g, downward positive) in response to an abrupt 4 times increase in atmospheric CO_2 concentration from CM4.0, SPEAR, SPEAR-SV, and ESM2M simulations. As δT_g increases, δN_g decreases, indicating a negative feedback from warming, which dampens the original perturbation of δN_g due to the abrupt increase in CO_2. While SPEAR exhibits a similar increase in δT_g as CM4.0, its reduction in δN_g is larger after the first 50 years, indicating a stronger negative feedback and faster approach toward the equilibrium state. By contrast, SPEAR-SV shows a smaller increase in δT_g than SPEAR and CM4.0, with a relatively similar drop in TOA flux as SPEAR, indicating that the dynamical vegetation in CM4.0 and SPEAR may give rise to additional positive effective radiative forcing or feedback, and thus more warming. Compared to the new generation GFDL models, ESM2M produces much less warming despite a similar reduction in δN_g over time, indicating much stronger negative feedback in ESM2M.

Figure 1b shows a scatterplot of δN_g versus δT_g from each model. The dashed and solid lines are respectively a linear regression based on the first 50 years and the last 100 years of the simulations. All models show a significant reduction in the slope, indicating an increase (less negative) in TOA net radiative feedback with time. The intercepts of the solid lines with the x axis divided by 2 (because 4xCO_2 is typically used instead of 2xCO_2 in this kind of simulations in CMIP6) provide an estimate of the EffCS for each model (e.g., Gregory et al. 2004; Winton et al. 2019). Based on these estimates, the EffCS of CM4.0, SPEAR, SPEAR-SV, and ESM2M are respectively 5, 4.2, 3.8, and 2.9 K. Compared to SPEAR-SV, CM4.0 produces ~32% [(5 − 3.8)/3.8] higher EffCS, among which roughly 1/3 of the increase is due to dynamical vegetation with rest of the increase (2/3) resulting from their difference in ocean and sea ice models. Compared to ESM2M, CM4.0 produces ~72% [(5 − 2.9)/2.9] higher EffCS, which may be surprising considering that the two models exhibit similar Cess sensitivity in their uncoupled atmospheric simulations with uniform SST warming. Table 3 provides a list of the models, including their components and the estimates of climate sensitivity using Cess and the abrupt 4xCO_2 simulations.

In Fig. 1, we have also plotted δT_g and δN_g from two uncoupled AM4.0 simulations (AM4-CM4-4xCO_2-50 and AM4-CM4-4xCO_2-125) using AM4-CM4-C as control with prescribed SST, SIC, vegetation, and CO_2 concentration derived from two periods [centered at year 50 (Y50) and year 125 (Y125)] of CM4.0's 4xCO_2 simulation and its pi-Control (see Table 1 for a description of the simulations). They reproduce well CM4.0's global SAT and TOA flux response to 4xCO_2 increase, indicating that the uncoupled AM4.0 simulations capture essential aspects of the climate changes and feedbacks in CM4.0 and may be used to understand CM4.0's forcing and feedback mechanisms and therefore EffCS.

Figures 2a and 2b show respectively the spatial distribution of SAT anomalies (δT) averaged from years 26–75 (Y50) and years 101–150 (Y125) of CM4.0's 4xCO_2 simulation compared to its pi-Control. Figure 2c shows the difference in δT between the two periods (Y125 minus Y50). There is generally

TABLE 3. A list of the coupled models, their components, and estimates of climate sensitivities using Cess (uniform 2-K SST warming) and abrupt 4xCO_2 simulations. The numbers in parentheses indicate the models' horizontal resolutions. A constant 4 W m^{-2} effective radiative forcing (ERF) for 2xCO_2 is used to estimate the Cess sensitivity for all models. The effective climate sensitivity (EffCS) is derived from a coupled model's abrupt 4xCO_2 and its corresponding pi-Control simulations using the Gregory method with two separate linear regressions (i.e., the first 50 years and the last 100 years).

Model	CM4.0	SPEAR	SPEAR-SV	ESM2M
Atmosphere	AM4.0 (100 km)	AM4.0 (100 km)	AM4.0 (100 km)	AM2 (200 km)
Land + vegetation	LM4.0 + DynVeg	LM4.0 + DynVeg	LM4.0 + StaticVeg	LM3.0 + DynVeg
Ocean	MOM6 (1/4°)	MOM6 (1°)	MOM6 (1°)	MOM4.1 (1°)
Sea ice	SIS2 (1/4°)	SIS2 (1°)	SIS2 (1°)	SIS1 (1°)
Cess sensitivity	2.56 K	2.56 K	2.56 K	2.48 K
EffCS	5 K	4.2 K	3.8 K	2.9 K

enhanced warming over land and the Northern Hemisphere (NH) high latitudes, including the Arctic region. The Southern Hemisphere (SH) sea ice region, the Antarctic continent, the Southern Ocean, and the eastern Pacific tend to experience delayed warming. While the warming pattern is broadly similar among the models, there are substantial differences in the magnitude of warming over the NH and SH high latitudes. To elucidate this, Figs. 2d–l show various intermodel differences in δT for each period and their corresponding differences in δT between the two periods. Compared to SPEAR, CM4.0 produces more (less) warming over the SH (NH) sea ice regions, especially during the late period indicating significant differences in sea ice change between the two models (Figs. 2d,e). Compared to SPEAR-SV, SPEAR produces more warming over the NH high-latitude land and the surrounding Arctic Ocean (Figs. 2g,h). It indicates that the incorporation of dynamical vegetation model into SPEAR (and CM4.0) can lead to a 2–4-K increase in SAT over a broad region of the NH high latitudes with the global mean SAT increased by 0.63 K (0.37 K) for the later (earlier) period. Despite the large differences over the NH and SH high latitudes, the differences in δT (and δSST; see supplementary Fig. 1 in the online supplemental material) over the broad open ocean are modest among CM4.0, SPEAR, and SPEAR-SV. This is however not true if we compare δT (or δSST) between CM4.0 and ESM2M. Compared to ESM2M, CM4.0 produces not only much larger global mean warming but also a substantial change in warming patterns (Figs. 2j,k and supplementary Figs. 1j,k). In particular, CM4.0 produces more warming over the eastern Pacific and the broader Southern Ocean. Figures 2f and 2i further show that the model differences in warming trends (i.e., the difference in δT between Y125 and Y50) over the broad open ocean remain relatively similar among CM4.0, SPEAR, and SPEAR-SV. However, ESM2M exhibits a much larger difference in its warming pattern trend. Specifically, Fig. 2l displays a broad hemispheric difference in the trends of warming pattern between CM4.0 and ESM2M, with CM4.0 generating more SH (less NH) warming trends than ESM2M. The large differences in δT, as well as its time evolution from Y50 to Y125 between CM4.0 and ESM2M, are due primarily to their differences in SST warming patterns (see supplementary Figs. 1j–l). We will come back to this in section 3c.

To explore climate feedbacks, we first decompose the total change in TOA net radiative flux N at any time and location (t, y, x) as

$$\delta N = \left(\frac{\partial N}{\partial \mathrm{CO_2}}\right)_{T_g} \delta \mathrm{CO_2} + \left(\frac{\partial N}{\partial T_g}\right)_{\mathrm{CO_2}} \delta T_g = F_{4\mathrm{xCO_2}} + \alpha \delta T_g, \quad (1)$$

where δ denotes the change from pi-Control to 4xCO_2 (i.e., 4xCO_2 minus pi-Control) and T_g represents the global mean SAT and is a function of time only (subscript g indicates global mean value); $F_{4\mathrm{xCO_2}}$ denotes the effective radiative forcing (ERF) at the TOA after atmospheric temperatures, water vapor, and clouds are adjusted to the CO_2 increase while keeping SSTs and sea ice conditions unchanged. α represents the feedback parameter. Both $F_{4\mathrm{xCO_2}}$ and α can be computed for each grid cell as well as the global mean.

In climate models with dynamical vegetation, $F_{4\mathrm{xCO_2}}$ may be further decomposed into two components:

$$F_{4\mathrm{xCO_2}} = F_{4\mathrm{xCO_2,noveg}} + F_{4\mathrm{xCO_2,veg}}, \quad (2)$$

where $F_{4\mathrm{xCO_2,noveg}}$ denotes the component of ERF independent from vegetation change while $F_{4\mathrm{xCO_2,veg}}$ denotes the component of ERF due only to the vegetation change that results from CO_2 fertilization and CO_2-induced changes in evapotranspiration (stomatal contraction) instead of temperature. The term $F_{4\mathrm{xCO_2,noveg}}$ may be assessed using an uncoupled atmospheric simulation with a quadrupling of atmospheric CO_2 concentration (AM4-CM4-4xCO_2-50 or AM4-CM4-4xCO_2-125) while keeping everything else (i.e., SSTs, SICs, vegetation, and others) unchanged from its control simulation (AM4-CM4-50 or AM4-CM4-125). The term $F_{4\mathrm{xCO_2,veg}}$ can be assessed using a pair of uncoupled AM4.0 simulations with the dynamical vegetation model turned on and fed with two different values of CO_2 concentrations (AM4-CM4-C-DVEG vs AM4-CM4-C-DVEG-4xCO_2) while keeping everything else identical to AM4-CM4-C. Because the global mean SAT (T_g) can still change in the pairs of uncoupled AM4.0 simulations with fixed SSTs and SICs due to land temperature response to changes in CO_2 or vegetation, we follow Hansen et al. (2005) to write the change of TOA flux in response to 4xCO_2 in the uncoupled AM4.0 as

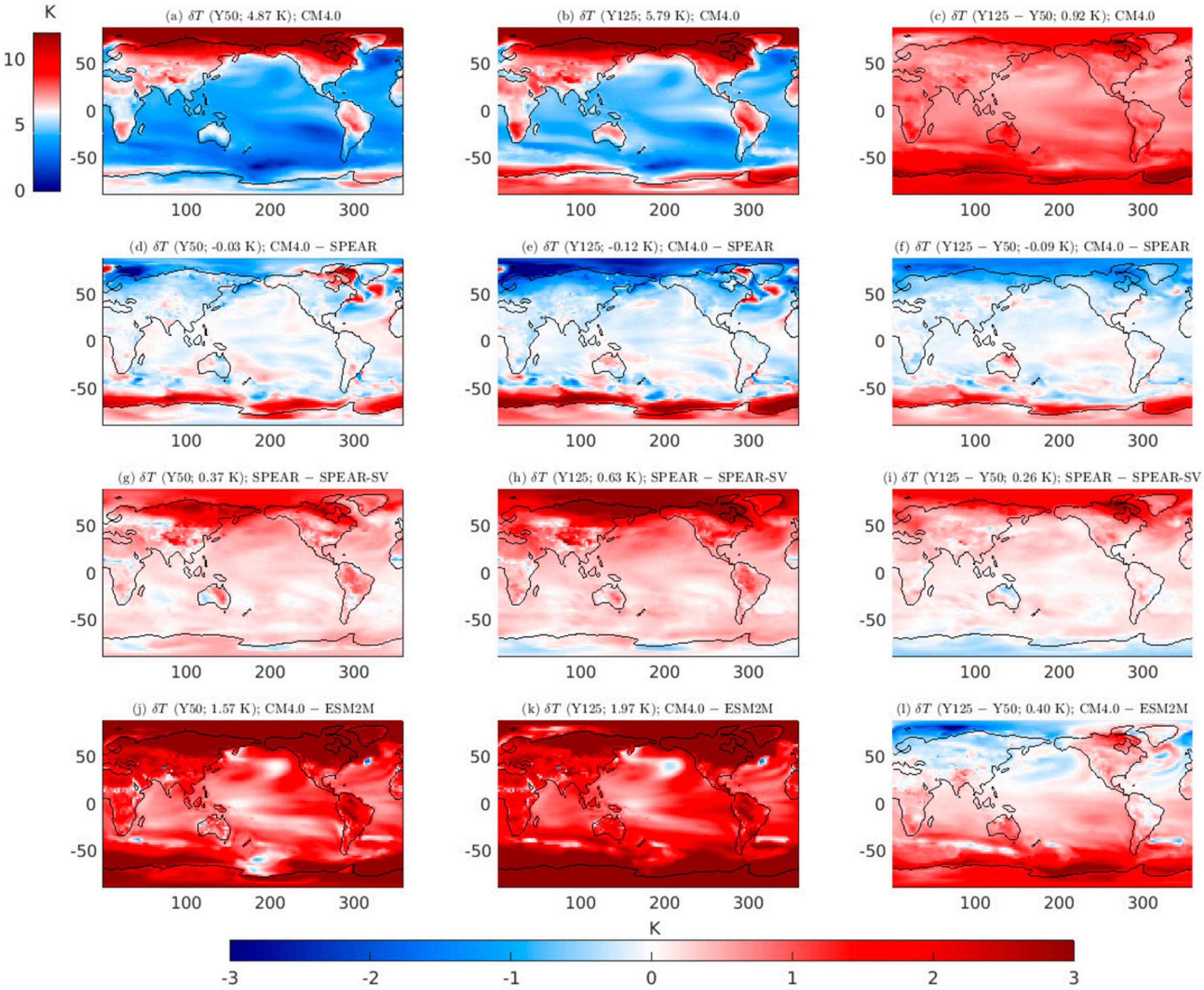

FIG. 2. (a)–(c) Geographical distribution of the change in surface air temperature (δT) between CM4.0's pi-Control and its 4xCO_2 simulation averaged from (a) years 26–75 (Y50) and (b) years 101–150 (Y125) period. (c) The difference in δT between (b) and (a) (Y125 − Y50). (d)–(f) As in (a)–(c), but showing the corresponding difference in δT between CM4.0 and SPEAR. (g)–(i) As in (d)–(f), but for the difference in δT between SPEAR and SPEAR-SV. (j)–(l) As in (d)–(f), but for the difference in δT between CM4.0 and ESM2M. Note that (a) and (b) use the color bar at the left while the rest of the panels use the color bar at the bottom. The global area-weighted mean from each map is shown on the top of each panel.

$$\Delta N_{4\mathrm{xCO_2,noveg}} = F_{4\mathrm{xCO_2,noveg}} + \alpha \Delta T_{g,\mathrm{noveg}}, \tag{3}$$

$$\Delta N_{4\mathrm{xCO_2,veg}} = F_{4\mathrm{xCO_2,veg}} + \alpha \Delta T_{g,\mathrm{veg}}, \tag{4}$$

where $\Delta N_{4\mathrm{xCO_2,noveg}}$ and $\Delta T_{g,\mathrm{noveg}}$ denote respectively the change in TOA net flux at any location (y, x) and global mean SAT change between AM4-CM4-50 (AM4-CM4-125) and AM4-CM4-4xCO_2-50 (AM4-CM4-4xCO_2-125). Similarly, $\Delta N_{4\mathrm{xCO_2,veg}}$ and $\Delta T_{g,\mathrm{veg}}$ denote respectively the change in TOA net flux and global mean SAT change between AM4-CM4-C-DVEG and AM4-CM4-C-DVEG-4xCO_2. The sum of Eqs. (3) and (4) can be used to assess the total ERF $F_{4\mathrm{xCO_2}}$:

$$\Delta N_{4\mathrm{xCO_2}} = F_{4\mathrm{xCO_2}} + \alpha \Delta T_{g,4\mathrm{xCO_2}}, \tag{5}$$

where $\Delta N_{4\mathrm{xCO_2}} = \Delta N_{4\mathrm{xCO_2,noveg}} + \Delta N_{4\mathrm{xCO_2,veg}}$, and $\Delta T_{g,4\mathrm{xCO_2}} = \Delta T_{g,\mathrm{noveg}} + \Delta T_{g,\mathrm{veg}}$. Combining Eqs. (1) and (5) and assuming α has the same value in both equations, $\alpha(t, y, x)$ may be obtained as

$$\alpha = \frac{\delta N - \Delta N_{4\mathrm{xCO_2}}}{\delta T_g - \Delta T_{g,4\mathrm{xCO_2}}}. \tag{6}$$

To the extent that $\Delta T_{g,4\mathrm{xCO_2}}$ is small relative to δT_g and might be ignored, $F_{4\mathrm{xCO_2}}$ might be approximated by $\Delta N_{4\mathrm{xCO_2}}$ and then the feedback parameter might be simply estimated as $\alpha = (\delta N - \Delta N_{4\mathrm{xCO_2}})/\delta T_g$.

Before we present the geographical distribution of $\Delta N_{4\mathrm{xCO_2,noveg}}$ and $\Delta N_{4\mathrm{xCO_2,veg}}$, we first show in Fig. 3a the time evolution of the change in global area-weighted mean leaf area index (LAI) from

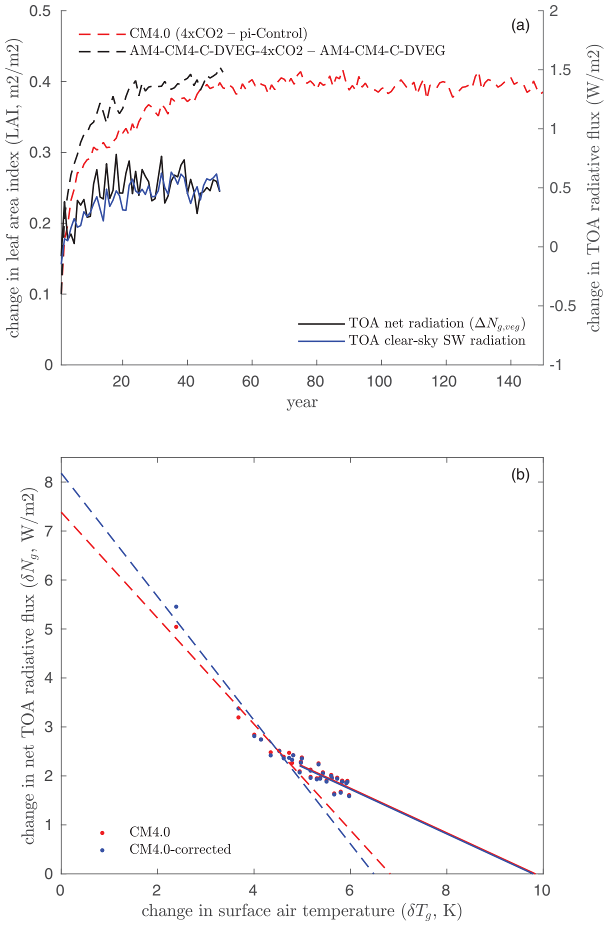

FIG. 3. (a) Left ordinate/legend: Time evolution of the change in global area-weighted mean leaf area index (LAI) from CM4.0's $4xCO_2$ simulation compared to its pi-Control (red dashed) and AM4-CM4-C-DVEG-$4xCO_2$ compared to AM4-CM4-C-DVEG (black dashed) (see Table 1 for a description of the simulations). Right ordinate/legend: Time evolution of the change in global net TOA radiative flux and its clear-sky SW component between AM4-CM4-C-DVEG-$4xCO_2$ and AM4-CM4-C-DVEG. (b) A comparison of the CM4.0 result from Fig. 1b (red) with a corrected regression identical to CM4.0 except with δN_g being replaced by $\delta N_g - \Delta N_{g,\mathrm{veg}} + \overline{\Delta N_{g,\mathrm{veg}}}$ (blue), where $\Delta N_{g,\mathrm{veg}}$ is from (a) and the overbar denotes time average (note $\Delta N_{g,\mathrm{veg}}$ values after year 50 is assumed to be a constant computed by averaging the last 30 years of $\Delta N_{g,\mathrm{veg}}$).

CM4.0's $4xCO_2$ simulation compared to its pi-Control and that from AM4-CM4-C-DVEG-$4xCO_2$ compared to AM4-CM4-C-DVEG. In CM4.0, the global LAI increases rapidly during the first 20 years and gradually stops increasing after roughly year 50 although substantial changes in regional LAI remain after year 50 (e.g., around the coast regions of the Arctic Ocean; see supplementary Figs. 2c,f). This indicates that most of the change in global LAI in CM4.0 may result from CO_2 fertilization and CO_2-induced change in evapotranspiration (stomatal contraction) rather than temperature-mediated feedback. This is confirmed by the difference in global LAI between AM4-CM4-C-DVEG-$4xCO_2$ and AM4-CM4-C-DVEG, which shows a similar increase even though both simulations are forced by the same SSTs and SICs. In fact, the global LAI in AM4-CM4-C-DVEG-$4xCO_2$ rises at a rate faster than that from CM4.0's $4xCO_2$ simulation, indicating that the temperature-mediated vegetation feedback may have slowed down the global LAI increase. In this uncoupled AM4.0, it takes 20–30 years for the global LAI to equilibrate with the abrupt increase of CO_2. As a result, it takes roughly 20–30 years for the global TOA radiation to reach an equilibrium state with a global mean forcing of ~0.48 W m^{-2} K^{-1} (Fig. 3a). This size of vegetation forcing is ~6% of the $4xCO_2$ forcing without considering vegetation adjustment. However, the increase in EffCS due to dynamical vegetation is roughly 10%, indicating that some specific features of vegetation forcing and/or additional temperature-mediated vegetation feedback may also be important. For example, vegetation forcing is concentrated over land, which might cause a stronger temperature response due to its lower heat capacity (than the ocean). We will leave an investigation of this to future work. The much longer time scale of vegetation adjustment to CO_2 increase is also very different from other fast processes such as the stratosphere and clouds adjustment. It may obscure the estimate of forcing and feedback using the simple regression method shown in Fig. 1b, especially during the earlier period of the $4xCO_2$ simulation. To illustrate this, Fig. 3b compares the regression of CM4.0's δN_g versus δT_g with a similar regression except with δN_g replaced by $\delta N_g - \Delta N_{g,\mathrm{veg}} + \overline{\Delta N_{g,\mathrm{veg}}}$, where $\Delta N_{g,\mathrm{veg}}$ is from the solid black line in Fig. 3a ($\Delta N_{g,\mathrm{veg}}$ values after year 50 are assumed to be a constant computed from the average of the last 30 years of $\Delta N_{g,\mathrm{veg}}$), and the overbar denotes the time average. The corrected regression (blue) yields a larger ERF and more negative feedback during the first 50 years with little impact on the regression after year 50 compared to the original regression (red, the CM4.0 result in Fig. 1b), which does not consider the slowly varying vegetation forcing in response to the abrupt increase of CO_2.

We now present in Figs. 4a and 4c the geographical distribution of $\Delta N_{4xCO_2,\mathrm{noveg}}$ and $\Delta T_{\mathrm{noveg}}$ computed by averaging two pairs of uncoupled AM4.0 $4xCO_2$ perturbation simulations in which we used the same static vegetation field derived from CM4.0's pi-Control (i.e., AM4-CM4-50 vs AM4-CM4-$4xCO_2$-50 and AM4-CM4-125 vs AM4-CM4-$4xCO_2$-125). The global mean value of $\Delta N_{4xCO_2,\mathrm{noveg}}$ differs slightly (8.31 vs 8.15 W m^{-2}) between the two pairs of simulations with both yielding a similar value of $\Delta T_{g,\mathrm{noveg}}$ (0.35 vs 0.36 K). Figures 4b and 4d show $\Delta N_{4xCO_2,\mathrm{veg}}$ and ΔT_{veg} derived from AM4-CM4-C-DVEG and AM4-CM4-C-DVEG-$4xCO_2$. The spatial distribution of $\Delta N_{4xCO_2,\mathrm{veg}}$ and ΔT_{veg} is highly inhomogeneous over the land with a global mean value of 0.48 W m^{-2} and 0.15 K respectively. It is interesting to note that the spatial distribution of $\Delta N_{4xCO_2,\mathrm{veg}}$ does not necessarily correspond well with that of ΔT_{veg}, especially over tropical Africa and the Amazon. This is because the increase in ΔT_{veg} and the effect of CO_2 on plants' evapotranspiration dry the atmospheric boundary layer and affect moist convection. In particular, there is an increase in outgoing LW radiation and a reduction in convective precipitation (not shown) which

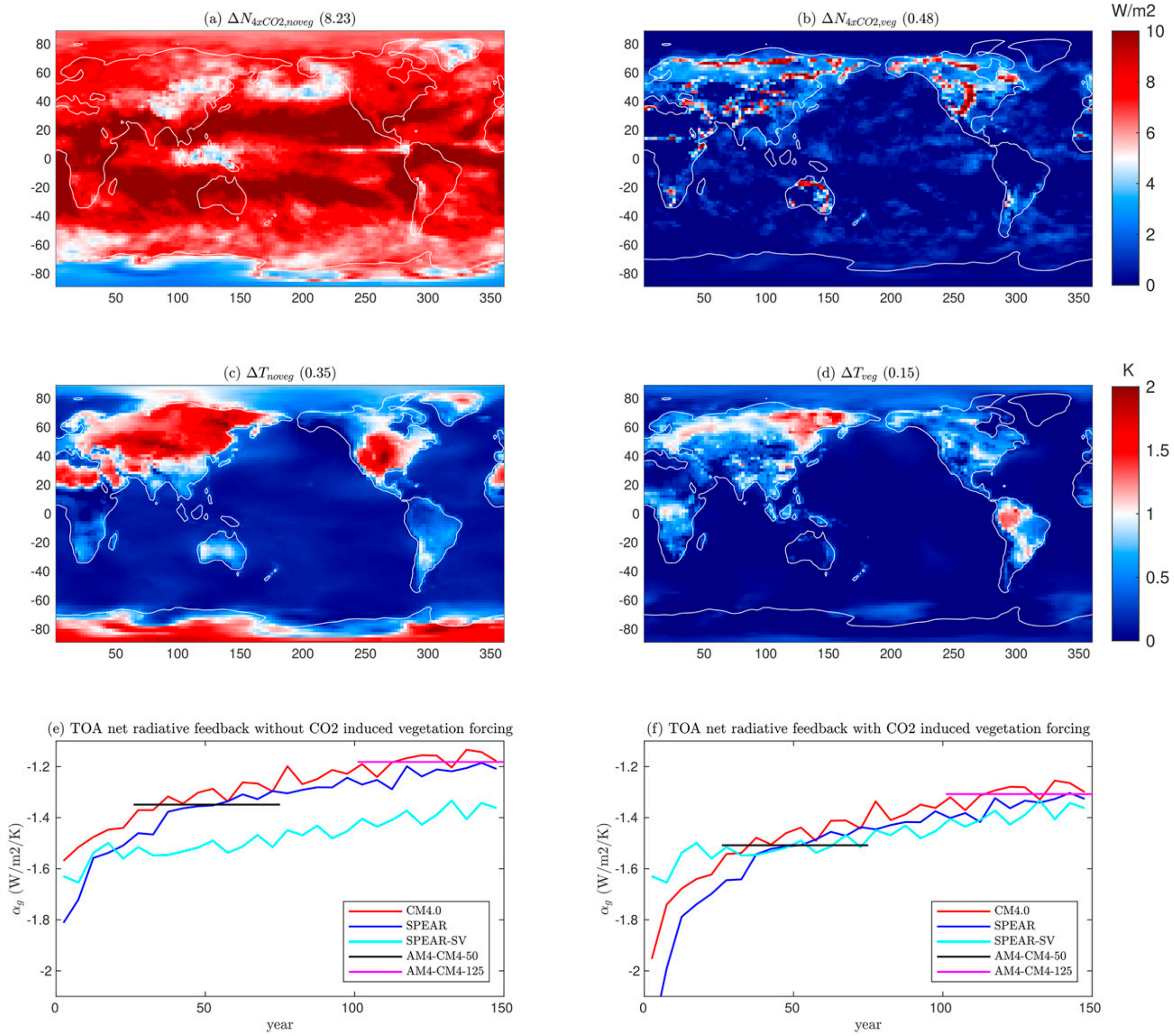

FIG. 4. (a) Geographical distribution of $\Delta N_{4xCO_2,noveg}$ computed by averaging two pairs of uncoupled AM4.0 4xCO_2 perturbation simulations in which we used the same static vegetation field derived from CM4.0's pi-Control (i.e., AM4-CM4-50 vs AM4-CM4-4xCO_2-50 and AM4-CM4-125 vs AM4-CM4-4xCO_2-125). The global area-weighted mean is shown at the top of the panel. (b) As in (a), but for $\Delta N_{4xCO_2,veg}$ computed by averaging the last 30 years of the difference between AM4-CM4-C-DVEG-4xCO_2 and AM4-CM4-C-DVEG. (c) As in (a), but for changes in surface air temperature (SAT) ΔT_{noveg}. (d) As in (b), but for changes in SAT ΔT_{veg}. (e) Time evolution of global TOA net radiative feedback (α_g) from CM4.0, SPEAR, and SPEAR-SV without considering the direct effect of CO_2 on vegetation [i.e., α_g is computed using Eq. (6)] with ΔN_{4xCO_2} and $\Delta T_{g,4xCO_2}$ obtained from (a) and (c) respectively. The horizontal lines show the TOA net radiative feedback derived from AM4-CM4-50 and AM4-CM4-125 simulations (using AM4-CM4-C as control without considering vegetation forcing). (f) As in (e), but with ΔN_{4xCO_2} and $\Delta T_{g,4xCO_2}$ including the direct effect of CO_2 on vegetation [i.e., using the sum of (a) and (b) [sum of (c) and (d)] for ΔN_{4xCO_2} ($\Delta T_{g,4xCO_2}$)]. The AM4-CM4-50 and AM4-CM4-125 results in (f) have also considered the radiative forcing and SAT change due to the direct effect of CO_2 on vegetation [i.e., (b) and (d)].

compensate for the increase in downward SW radiation at TOA and result in little change in TOA net radiative forcing over tropical Africa and the Amazon. Figure 4e plots the time evolution of global TOA net radiative feedback (α_g) from CM4.0, SPEAR, and SPEAR-SV without consideration of the CO_2-induced vegetation forcing [i.e., α_g is computed using Eq. (6) with ΔN_{4xCO_2} and $\Delta T_{g,4xCO_2}$ obtained from Figs. 4a and 4c respectively]. While α_g increases (less negative) with time for all three models, it appears to be substantially larger (less negative) in CM4.0 and SPEAR than in SPEAR-SV after the first 30 years. However, when the CO_2-induced vegetation forcing is considered in CM4.0 and SPEAR [i.e., α_g is computed using Eq. (6) with ΔN_{4xCO_2} and $\Delta T_{g,4xCO_2}$ obtained from the sum of Figs. 4a and 4b and the sum of Figs. 4c and 4d, respectively], their feedback values are much closer to those of SPEAR-SV (Fig. 4f). This indicates the importance of considering the CO_2-induced vegetation forcing to understand the models' difference in feedback. Note that because the vegetation forcing increases slowly in the first 20 years before it gradually reaches equilibrium, CM4.0's and SPEAR's feedback values in the first 20 years in Fig. 4f tend to have a negative bias (overly corrected), especially at the beginning of the simulations. This leads to a seemingly more rapid increase in feedback in CM4.0 and SPEAR during the first 20 years. After the first 50 years, CM4.0, SPEAR, and SPEAR-SV exhibit a relatively similar rate of increase in α_g, indicating that some common processes among the models may dominate the feedback increase.

The horizontal lines in Figs. 4e and 4f show the TOA net radiative feedback derived from the two pairs of uncoupled AM4.0 simulations (i.e., AM4-CM4-50 and AM4-CM4-125 using AM4-CM4-C as the control) with prescribed SSTs, SICs, and vegetation from CM4.0's pi-Control and $4xCO_2$ simulations. They agree reasonably well with the α_g values derived from the coupled simulation using Eq. (6) as long as the CO_2-induced vegetation forcing is consistently treated (i.e., not included in Fig. 4e and included in Fig. 4f). Note that in order to account for CO_2-induced vegetation forcing in uncoupled AM4.0 simulations with prescribed SSTs, SICs, and vegetation, we need to subtract Figs. 4b and 4d respectively from the changes in TOA radiation and SAT in AM4-CM4-50 (or AM4-CM4-125) using AM4-CM4-C as the control and then compute the feedback.

As shown in Figs. 1b, 3b, 4e, and 4f, the global feedback strength changes with time in the models especially after the first 50 years of the $4xCO_2$ simulation. However, the feedback parameter computed using Eq. (6) after the first 50 years still contains the impact of the feedback from the first 50 years (i.e., cumulative effect) because the TOA flux and SAT are compared against their pi-Control values. To investigate the feedback parameter after year 50, below we include a different definition of the feedback parameters by assuming two constant feedback parameters: $\alpha_1(y, x)$ for feedback before year 50 and $\alpha_2(y, x)$ after year 50. This is more consistent with the two linear regressions of Figs. 1b and 3b (e.g., Andrews et al. 2015; Winton et al. 2019). With this assumption, Eq. (1) can be rewritten as

$$\delta N(t,y,x) = \begin{cases} F_{4xCO_2}(y,x) + \alpha_1(y,x)\delta T_g(t) & \text{if} \quad t \le 50\ \text{yr} \\ \delta N(50,y,x) + \alpha_2(y,x)[\delta T_g(t) - \delta T_g(50)] & \text{if} \quad t > 50\ \text{yr} \end{cases}. \tag{7}$$

For years before year 50, Eq. (7) would be the same as Eq. (1). However, for years after year 50, it is the feedback parameter α_2 that determines the rate of global mean warming per unit decrease of TOA net radiation. Thus, α_2 is important for a model's EffCS because it controls the additional SAT warming after the first 50 years as the remaining TOA radiative imbalance continues to approach zero. However, because of the different definitions of the feedback parameter α_2, we do not expect it is the same as that defined in Eq. (6). We refer to Rugenstein and Armour (2021) for various definitions of the feedback parameters and their implications to ECS and/or EffCS. Below we compare the TOA net radiative feedback computed from years 26–75 and years 101–150 using Eq. (6) as well as α_2 using Eq. (7) based on the two periods.

Figures 5a, 5d, and 5g show the geographical distribution of α derived from years 26–75 of the $4xCO_2$ simulation and its corresponding pi-Control from CM4.0, SPEAR and SPEAR-SV respectively. While there is a broad similarity in the spatial distribution of α among the three models, CM4.0 displays substantially larger positive feedback over the SH sea ice–covered region near the Antarctic continent. Compared to SPEAR-SV, both CM4.0 and SPEAR produce more positive feedback over the NH high-latitude lands near the Arctic Ocean (which are typically dominated by tundra in the present climate) and more negative feedback in lower-latitude Eurasia and North America. Figure 5j demonstrates that locally, the vegetation feedback can amount to ±3 $W\ m^{-2}\ K^{-1}$ in this model. Indeed, there is a large increase in LAI over the NH high-latitude land in CM4.0 and SPEAR in response to the $4xCO_2$ increase (see supplementary Figs. 2a,d), due presumably to the fact that these regions have the smallest LAI (and coldest SAT) in their pi-Control but experience the largest SAT warming in the $4xCO_2$ simulations (see Figs. 2a,b). In addition, these regions exhibit the largest percentage increase in surface precipitation, which would also help vegetation to grow. The increase in LAI causes more downward shortwave radiation into the NH high-latitude land surface, which is typically covered by snow (see supplementary Figs. 2g,j). The impact of vegetation on snow albedo is related to the amount of vegetation able to grow above the snow masking depth in GFDL's land model. However, as shown in Fig. 3, the global LAI response to $4xCO_2$ increase is due primarily to CO_2 fertilization and CO_2-induced changes in evapotranspiration (stomatal contraction) rather than a temperature-mediated feedback. When CO_2-induced vegetation forcing is removed from the feedback calculations (i.e., Figs. 5a–f), the difference in global mean feedback between SPEAR and SPEAR-SV is fairly small despite the substantial increases and decreases in regional feedback (see Fig. 5j).

Figures 5b, 5e, and 5h further display the α values derived from the last 50 years of each model's $4xCO_2$ simulation and its corresponding pi-Control. The spatial patterns are similar to those from the earlier period despite increased (less negative) global mean feedbacks. This is because the feedbacks computed using Eq. (6) are dominated by the earlier period, which produces the most reduction (warming) in δN (δT_g). Figure 5k shows that the global feedback difference between SPEAR and SPEAR-SV remained small for the last 50 years with a pattern similar to that in Fig. 5j. It is consistent with Fig. 3a, which shows that the global LAI stops increasing after year 50 despite the

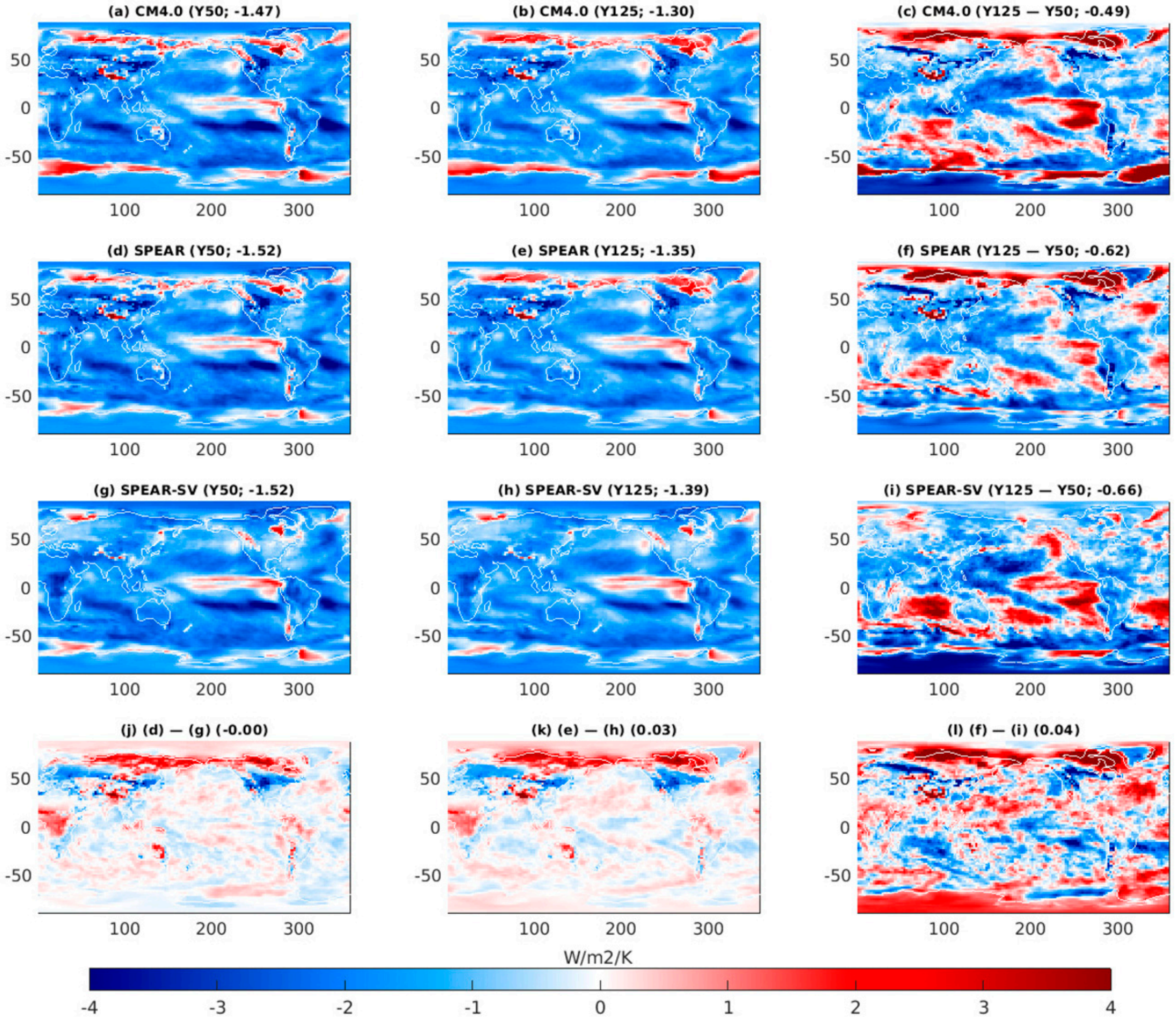

FIG. 5. (a)–(c) Geographical distribution of TOA net radiative feedback α in response to global mean surface air temperature warming (W m^{-2} K^{-1}) derived [using Eq. (6), the sum of Figs. 4a and 4b for $\Delta N_{4\mathrm{xCO}_2}$ and the sum of Figs. 4c and 4d for $\Delta T_{g,4\mathrm{xCO}_2}$] from (a) years 26–75 (Y50) and (b) years 101–150 (Y125) period of CM4.0's 4xCO$_2$ simulation and its pi-Control. (c) TOA feedback α_2 computed using Eq. (7) and the two periods centered at year 50 and year 125 (Y125 − Y50). The global mean value is shown on the top of each panel. (d)–(f) As in (a)–(c), but for SPEAR. (g)–(i) As in (a)–(c), but for SPEAR-SV. Note that for SPEAR-SV only Figs. 4a and 4b are used for $\Delta N_{4\mathrm{xCO}_2}$ and $\Delta T_{g,4\mathrm{xCO}_2}$ respectively because dynamical vegetation is not used in this model. (j)–(l) As in (d)–(f), but showing the difference between SPEAR and SPEAR-SV to highlight the impact of dynamic vegetation on temperature mediated feedback.

fact that LAI around the coastal regions of the Arctic Ocean still increases with compensating reductions at the lower latitudes of North America and Eurasia (see supplementary Figs. 2c,f).

Finally, Figs. 5c, 5f, and 5i show the feedback parameter α_2 computed using the difference between the two periods (centered at Y50 vs Y125) based on Eq. (7). In contrast to Figs. 5b, 5e, and 5h, there is a much larger increase (less negative) in global TOA feedback for all models. Spatially, the increase is dominated by the eastern Pacific and the broader SH oceans. This increase is caused primarily by an increase in cloud feedback, which may be estimated by changes in TOA net cloud radiative effect (CRE; see supplementary Figs. 3a–i). We note that the change in CRE per degree of global SAT warming is not strictly speaking the "cloud feedback" because it does not account for cloud masking of the clear-sky response (Soden et al. 2004). However, this measure is highly correlated with cloud feedback computed using the partial radiative perturbation (PRP) method with a systematic difference of 0.3–0.4 W m^{-2} K^{-1} (Soden et al. 2004). It has been widely used in the climate analysis community to infer intermodel differences in cloud feedback (e.g., Cess et al. 1990, 1996; Bony et al. 2004; Bony and Dufresne 2005; Wyant et al. 2006; Medeiros et al. 2008; Andrews et al. 2012; Webb et al. 2013; Zhang et al. 2013; Ringer et al. 2014; Webb et al. 2015;

Bretherton 2015; Silvers et al. 2018; Wing et al. 2020). This is because it is readily available from model output and, with clear-sky feedback, it adds up to the modeled total TOA feedback. In this paper, we follow the previous studies and simply refer to it as cloud feedback. We will return to the cloud feedback in section 3c. Here, it is also interesting to note that compared to SPEAR and SPEAR-SV, CM4.0 produces substantially higher α_2 over the Antarctic sea ice regions, which contributes to its higher (less negative) global mean α_2. In addition, CM4.0 and SPEAR produce a higher α_2 over the Arctic coast than SPEAR-SV, although the global mean α_2 differs only slightly between SPEAR and SPEAR-SV. Because α_2 has removed the feedback effect from the earlier period (the first 50 years) and measures the actual feedback each model experiences during the later period of their $4xCO_2$ simulations, Figs. 5c, 5f, and 5i would be more relevant to the models' ECS than Figs. 5b, 5e, and 5h, assuming the feedback parameters remain constant as the models continue to equilibrate. However, we note that α_2 is not the same as the feedback parameter one traditionally uses to define ECS because it does not satisfy the relationship ECS = $-F_{2xCO_2}/\alpha$ (Rugenstein and Armour 2021).

To further understand the causes of model differences in TOA feedback, we show in Fig. 6 the intermodel differences in latitudinal distribution of TOA net radiative feedback, as well as its decomposition into individual components derived from years 101–150 of the $4xCO_2$ simulation and its corresponding pi-Control from CM4.0, SPEAR, SPEAR-SV, and ESM2M. Note the direct effect of $4xCO_2$ on TOA radiation and SAT has been removed to compute the total feedback as well as its individual components. For each individual component, δN and ΔN_{4xCO_2} in Eq. (6) are replaced by the corresponding component derived from the same set of $4xCO_2$ perturbation experiments used for computing δN and ΔN_{4xCO_2} (see Figs. 4a,b). The feedback difference between CM4.0 and SPEAR (red lines) occurs primarily over the Antarctic sea ice region and is dominated by the clear-sky SW component (Fig. 6d) with the clear-sky LW component (Fig. 6c) slightly counteracting the SW component. In contrast, the cloud feedback difference between CM4.0 and SPEAR is generally small and subtle (Fig. 6b). Indeed, Fig. 6e shows that compared to SPEAR, CM4.0 produces a substantially larger reduction in SICs over the Antarctic sea ice region and somewhat a smaller reduction in SICs over the Arctic region, which well explains their difference in clear-sky SW feedback. The feedback difference between SPEAR and SPEAR-SV (green lines) occurs primarily over the NH high latitudes featuring a northward shift of positive feedback (Fig. 6a). This is also due primarily to the clear-sky SW feedback (see Fig. 6d). The SIC difference between SPEAR and SPEAR-SV is generally small except in the Arctic, where SPEAR produces a larger SIC reduction due presumably to the surrounding land warming associated with vegetation increase. Indeed, Fig. 6f shows that compared to SPEAR-SV, CM4.0 and SPEAR produce a temperature-mediated LAI feedback featuring a northward shift of vegetation from the middle to high latitudes in NH, which is independent of the direct response of vegetation to CO_2 increase. This leads to an increase in net shortwave radiation into land surface in NH higher latitudes and a reduction in the lower latitudes (green dashed lines in Fig. 6f) due to the effect of vegetation on snow albedo. This explains the difference in clear-sky SW feedback between SPEAR and SPEAR-SV (Fig. 6d). Despite the large difference in latitudinal distribution of the vegetation feedback, the global mean feedback between SPEAR and SPEAR-SV is relatively small compare to other feedbacks. In general, the feedback difference between CM4.0 and SPEAR-SV is dominated by their difference in SH sea ice feedback and the vegetation feedback over the NH high latitudes.

Finally, Fig. 6 also displays the feedback difference between CM4.0 and ESM2M. Compared to the differences among CM4.0, SPEAR, and SPEAR-SV, ESM2M stands out by its much smaller (less positive or more negative) cloud feedback over most latitudes (Fig. 6b). In addition, ESM2M also exhibits a much smaller reduction in SH SICs (Fig. 6e) and therefore much less positive clear-sky SW feedback over the Antarctic sea ice region (Fig. 6d). Globally, compared to ESM2M, CM4.0 produces a 0.86 $W m^{-2} K^{-1}$ increase (less negative) in global mean TOA net feedback, out of which 0.42 $W m^{-2} K^{-1}$ is from cloud feedback and 0.23 $W m^{-2} K^{-1}$ is from clear-sky SW feedback, with the rest from clear-sky LW feedback. This indicates that cloud feedback is the leading cause of the increase in EffCS in CM4.0 compared to ESM2M despite playing little role in explaining the intermodel differences in EffCS among CM4.0, SPEAR, and SPEAR-SV.

b. *Uncoupled AM4.0 simulations*

In the following, we attempt to use the uncoupled AM4.0 simulations to isolate the feedbacks associated with changes in SST, SIC, and vegetation in CM4.0's $4xCO_2$ simulation. Figures 7a and 7b show the geographical distribution of TOA net feedback parameter α derived from AM4-CM4-50 and AM4-CM4-125 (using AM4-CM4-C as control). The direct effect of $4xCO_2$ on vegetation and associated $\Delta N_{4xCO_2,\mathrm{veg}}$ and ΔT_{veg} (i.e., Figs. 4b,d) has been removed because part of the vegetation change between AM4-CM4-C and AM4-CM4-50 (or AM4-CM4-125) is due to the direct effect of $4xCO_2$ on vegetation rather than the temperature-mediated feedback. The pattern looks very similar to that shown in Figs. 5a and 5b with only a small difference in global mean values. This indicates that Eq. (6) can fairly well capture both the global mean and the geographical distribution of TOA net feedback from the coupled simulations provided that ΔN_{4xCO_2} and $\Delta T_{g,4xCO_2}$ are known. Furthermore, Fig. 7c shows that the feedback parameter α_2 derived from AM4-CM4-125 simulation (using AM4-CM4-50 as control) also agrees well with Fig. 5c, with both showing a large increase in global mean feedback compared to that from the earlier period (i.e., α_1 in Figs. 5a and 7a). However, uncoupled AM4.0 allows one to change SST, SIC, and vegetation in isolation so that the total feedback in Figs. 7a–c can be further partitioned into contributions from individual components. The contribution from each component is computed as the change in TOA net radiative flux from its corresponding component (SST, SIC, vegetation)

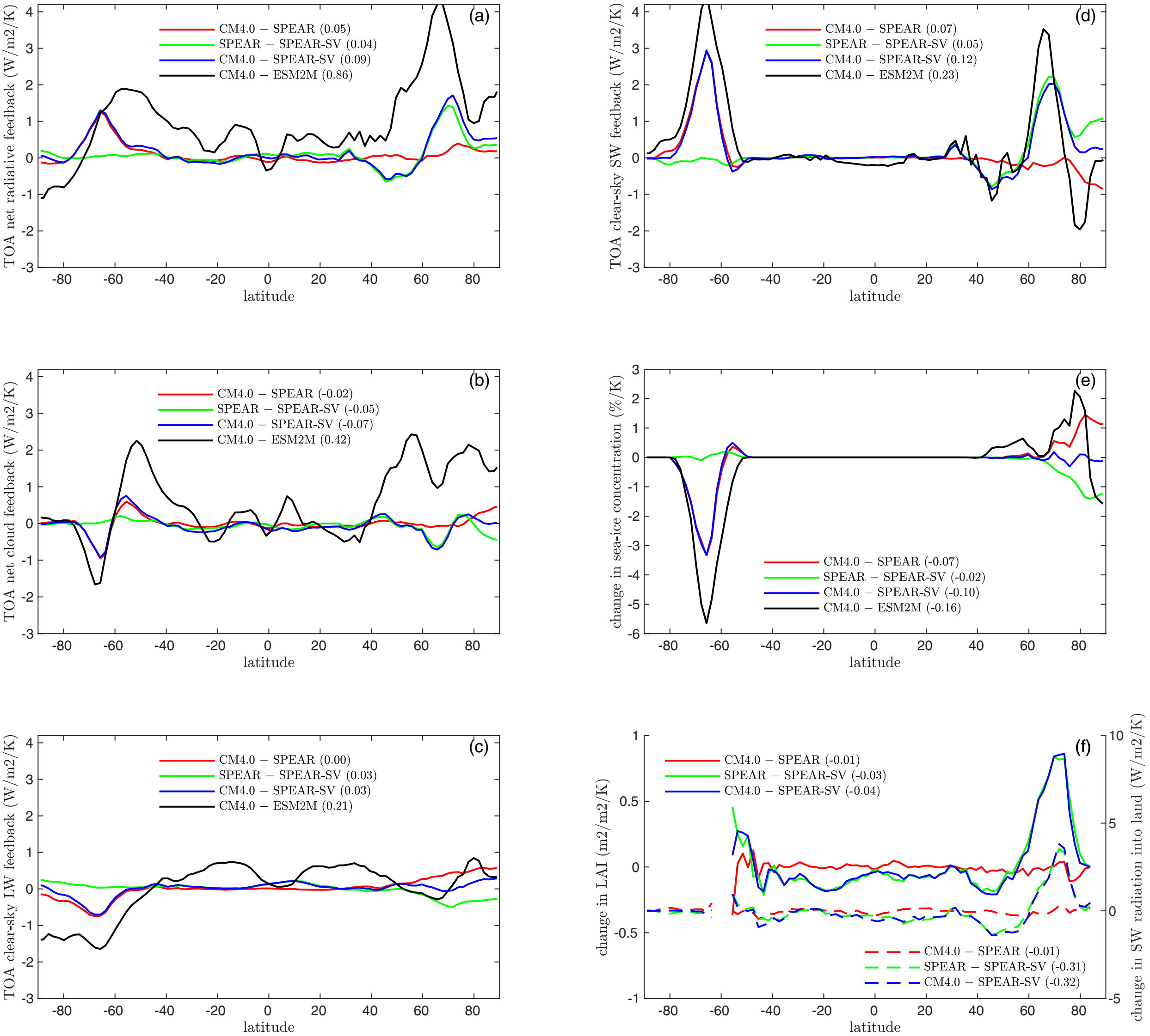

FIG. 6. Model differences (see legend) in latitudinal distribution of TOA (a) net radiative feedback, and its decomposition into (b) cloud, (c) clear-sky longwave, and (d) clear-sky shortwave feedbacks (W m^{-2} K^{-1}) derived [using Eq. (6)] from years 101–150 of the 4xCO_2 simulation and its corresponding pi-Control from CM4.0, SPEAR, SPEAR-SV, and ESM2M. Except for SPEAR-SV, the same $\Delta N_{4xCO_2,veg}$ (Fig. 4b) and $\Delta T_{g,veg}$ (Fig. 4d) are included in ΔN_{4xCO_2} and $\Delta T_{g,4xCO_2}$, respectively, for computing feedbacks in all models. SPEAR-SV only uses Fig. 4a for ΔN_{4xCO_2} and Fig. 4c for $\Delta T_{g,4xCO_2}$. For each individual component of the net feedback, δN and ΔN_{4xCO_2} in Eq. (6) are simply replaced by the corresponding component derived from the same set of 4xCO_2 perturbation simulations used for deriving δN and ΔN_{4xCO_2} (see Fig. 4 caption for details). The global area-weighted means are shown in the legend of each panel. (e) As in (d), but for sea ice concentration feedback. (f) As in (d), but for leaf area index (LAI; left ordinate) and net surface SW radiation (right ordinate, downward positive) feedback computed over the land covering regions at each latitude. The direct effect of 4xCO_2 on LAI and associated surface SW radiation has been removed following the same procedure as that for TOA radiation. The global land area weighted means are shown in the legend.

perturbation simulation normalized by the same global mean SAT change in Figs. 7a–c so that the sum of individual components roughly equals those shown in Figs. 7a–c. Note, for the vegetation perturbation simulations (i.e., Figs. 7j,k), the direct effect of 4xCO_2 on vegetation and its associated $\Delta N_{4xCO_2,veg}$ has been removed.

The contribution from changes in SST anomalies is shown in Figs. 7d–f. Except in the NH and SH high latitudes, the spatial pattern in TOA net feedback is determined primarily by SST warming anomalies, which may be further decomposed into a spatial pattern of SST anomalies and a global mean warming. Figure 7d shows a global mean feedback of -1.65 W m^{-2} K^{-1}, which is very similar to that (-1.66 W m^{-2} K^{-1}) from AM4-uniform2K (see Fig. 10j). This is likely because the SST anomalies, which are computed against pi-Control (AM4-CM4-C), are dominated by the global mean warming instead of a lack

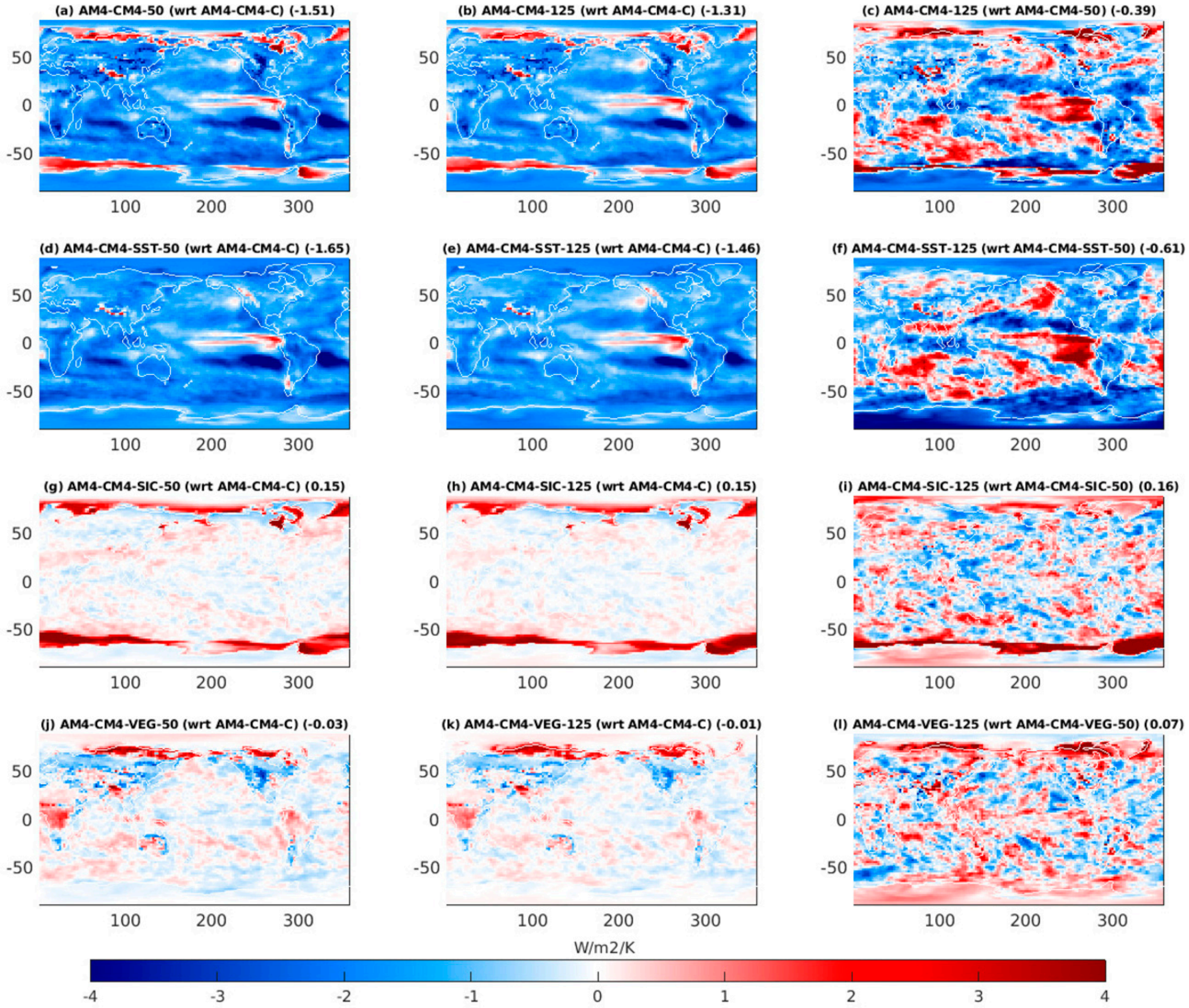

FIG. 7. (a)–(c) Geographical distribution of TOA net radiative feedback (W m^{-2} K^{-1}) derived from (a) AM4-CM4-50 and (b) AM4-CM4-125 using AM4-CM4-C as a control. (c) As in (b), except using AM4-CM4-50 as a control to estimate the feedback parameter α_2 after year 50 of CM4.0's 4xCO$_2$ simulation. (d)–(f) As in (a)–(c), but for feedback contributions from SST anomalies using AM4-CM4-SST-50 and AM4-CM4-SST-125. (g)–(i) As in (a)–(c), but for feedback contributions from SIC anomalies using AM4-CM4-SIC-50 and AM4-CM4-SIC-125. (j)–(l) As in (a)–(c), but for feedback contributions from vegetation anomalies using AM4-CM4-VEG-50 and AM4-CM4-VEG-125. The feedbacks in each column are computed as their corresponding change in TOA net radiative flux normalized by the same global mean SAT change. In (a), (b), (j), and (k) the direct effect of 4xCO$_2$ on vegetation and associated $\Delta N_{4\mathrm{xCO}_2,\mathrm{veg}}$ (i.e., Fig. 4b) has been removed. The global mean SAT change is 4.32 K (AM4-CM4-50 − AM4-CM4-C − $\Delta T_{g,\mathrm{veg}}$) for the left column, 5.26 K (AM4-CM4-125 − AM4-CM4-C − $\Delta T_{g,\mathrm{veg}}$) for the center column, and 0.94 K (AM4-CM4-125 − AM4-CM4-50) for the right column. The global mean feedback is shown on the top of each panel.

of feedback sensitivity to SST warming patterns in this model. Indeed, comparing Fig. 7f with Fig. 7c indicates that most of the total feedback increase between the earlier and later period (comparing Figs. 7a,c) is due to changes in SST warming pattern (comparing Figs. 7d,f). However, this large difference can only be well seen if we focus on the difference between the two periods (AM4-CM4-50 versus AM4-CM4-125) because using AM4-CM4-C as a control obscures the feedback estimate for the later period. We will return to the effects of SST warming pattern later.

Figures 7g–i show the TOA feedback contribution from changes in SICs. Using AM4-CM4-C as the control, the global mean feedback due to SIC change is roughly 0.15 W m^{-2} K^{-1} for both the earlier and later periods. Locally, the feedback strength can be 2–8 W m^{-2} K^{-1} with the largest positive feedback coming from some SH sea ice–covered regions. Figure 7i shows that the global mean SIC feedback (derived using AM4-CM4-50 and AM4-CM4-125) stays relatively unchanged after year 50, although it tends to be increasingly dominated by the feedback over the SH sea ice–covered

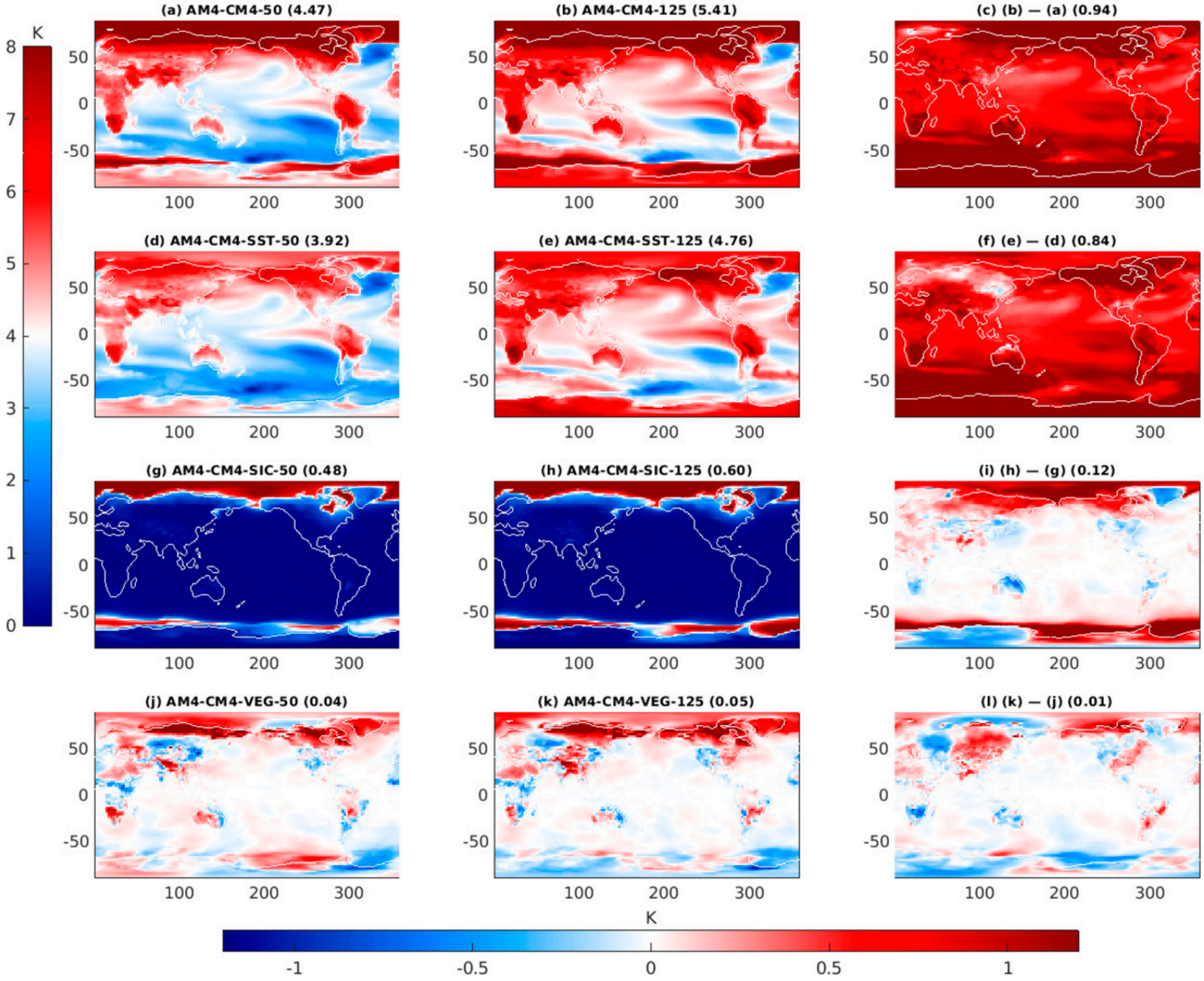

FIG. 8. (a)–(c) Geographical distribution of the change in surface air temperature (SAT) from (a) AM4-CM4-50 and (b) AM4-CM4-125 using AM4-CM4-C as a control. (c) The difference between (b) and (a) (AM4-CM4-125 minus AM4-CM4-50). (d)–(f) As in (a)–(c), but for SAT change associated with SST anomalies using AM4-CM4-SST-50 and AM4-CM4-SST-125. (g)–(i) As in (a)–(c), but for SAT change associated with SIC anomalies using AM4-CM4-SIC-50 and AM4-CM4-SIC-125. (j)–(l) As in (a)–(c), but for SAT changes associated with vegetation anomalies using AM4-CM4-VEG-50 and AM4-CM4-VEG-125. Note that (a), (b), (d), (e), (g), and (h) use the left color bar; the remaining panels use the bottom color bar. The global area-weighted mean is shown on the top of each panel. See Table 1 for a description of the simulations.

regions. The feedback maps computed using the two periods (i.e., AM4-CM4-50 and AM4-CM4-125) are generally noisier due to their much smaller change in global SAT (or SST) compared to their SAT (or SST) change from pi-Control (AM4-CM4-C). Finally, Figs. 7j–l show the TOA feedback from temperature-mediated changes in vegetation. Both the spatial pattern and the relatively small global mean feedback are consistent with the feedback difference between SPEAR and SPEAR-SV (Figs. 5j–l), indicating again that most of the impact of the dynamical vegetation model on CM4.0's (and SPEAR's) EffCS is due to an increased ERF rather than temperature mediated feedback.

In these uncoupled atmospheric simulations, a change in SICs or vegetation may modify the feedback parameters in two different ways if the system is linear to individual perturbations. One is through a change in TOA flux and the other through a change in global SAT. Figure 8 shows that the SAT change between AM4-CM4-C and AM4-CM4-50 (or AM4-CM4-125) is fairly linear when decomposed into contributions from SST, SIC, and vegetation anomalies with the global mean SAT changes in Figs. 8a–c (i.e., 4.47, 5.41, and 0.94 K) being very close to the sum of the three individual components (comparing each column of Fig. 8). If we add to Figs. 8a and 8b the global SAT change (0.35 K; see Fig. 4c) due to a fourfold increase of CO_2 concentration from the uncoupled AM4.0 simulations without vegetation change, the total SAT change also recovers well the global SAT change during the two periods of CM4.0's 4xCO_2 simulation (i.e., 4.87 and 5.79 K; see Figs. 2a,b). Comparing Fig. 7 and Fig. 8, SIC anomalies produce not only a significant increase in TOA flux (e.g., $0.79 = 0.15 \times 5.26$ W m^{-2};

see Fig. 7h) but also a substantial increase in global SAT (e.g., 0.6 K; see Fig. 8h). The sizable impact of SIC anomalies on global SAT changes indicates that the estimates of TOA feedback associated with the SST anomalies (i.e., Figs. 7d,e) are slightly larger (less negative) than those estimated by using the traditional SST-perturbation only simulations (e.g., Cess or SST warming pattern simulations in section 3c) because they do not consider any changes in SICs and the associated additional SAT warming in the denominator. In contrast, the global SAT changes associated with vegetation anomalies appear to be negligible.

c. *Uncoupled AM4.0 simulations with various SST warming patterns*

So far, we have explored the intermodel difference in EffCS among CM4.0, SPEAR, SPEAR-SV, and ESM2M and demonstrated that an increase in ERF associated with the dynamic vegetation model (Figs. 3 and 4) and an enhanced clear-sky SW feedback associated with a stronger reduction in Antarctic SICs (Figs. 6d,e) are the primary causes of the EffCS increase in CM4.0 compared to SPEAR-SV. While the temperature mediated change in vegetation has substantially regional impact on feedback its contribution to the global mean feedback is relatively small. The SST warming patterns among CM4.0, SPEAR, and SPEAR-SV are fairly similar (see supplementary Fig. 1), and they do not appear to play an important role in causing the model differences in feedback (Fig. 6). However, the change in SST warming patterns between the earlier and later periods of the model's 4xCO_2 simulation leads to a substantial increase in TOA net feedback and EffCS. Finally, it is worth noting that despite its sizable decrease in EffCS compared to CM4.0, SPEAR-SV still produces an EffCS of 3.8 K, which is substantially higher than ESM2M (2.9 K), indicating something else must be important in explaining the EffCS increase in the GFDL's new climate models. Indeed, Fig. 6b shows that while cloud feedback does not explain the key feedback differences among CM4.0, SPEAR, and SPEAR-SV, it appears to be the leading cause of the feedback difference between CM4.0 and ESM2M. As we noted before, the atmospheric model (AM2) used in ESM2M and AM4.0 produce a similar Cess sensitivity in response to uniform SST warming with the global mean cloud feedback differs only modestly (-0.04 W m^{-2} K^{-1} for AM2 and 0.13 W m^{-2} K^{-1} for AM4.0). However, the SST warming patterns (supplementary Fig. 1) produced by CM4.0 and ESM2M differ substantially. Below we explore to what extent the additional positive feedback and the EffCS increase in CM4.0 compared to ESM2M may be caused by their difference in SST warming patterns.

Figures 9a and 9b show the SST warming patterns derived from two different periods (AM4-CM4pattern2K-50 for years 26–75 and AM4-CM4pattern2K-125 for years 101–150) of CM4.0's 4xCO_2 simulation and its pi-Control. Except in the North Atlantic high-latitude regions, both show relatively more warming in the NH than in SH. The SST warming pattern in Fig. 9b looks similar to Fig. 9a because the SST differences between the later period and pi-Control are dominated by the earlier period. However, the warming pattern derived from the two periods (Fig. 9c; AM4-CM4pattern2K-125minus50) exhibits a distinct difference in the later period with relatively more warming in the southeastern Pacific and the broader Southern Ocean compared to the earlier period. Figures 9d–f show the SST warming patterns similarly derived as CM4.0 except from ESM2M's 4xCO_2 and pi-Control simulations. Compared to ESM2M, CM4.0 tends to produce more relative warming over the broad Southern Ocean, the eastern Pacific as well as the North Atlantic high-latitude regions (see Figs. 9g,h). Figure 9i further displays a broad hemispheric difference in the trend of warming pattern with relatively more (less) SH (NH) warming in CM4.0 than ESM2M during the later period of their 4xCO_2 simulations. To explore which features of SST warming pattern differences between CM4.0 and ESM2M are more important, we show in Fig. 9k a simulation (AM4-CM4pattern2K-125-modified) similar to Fig. 9b (AM4-CM4pattern2K-125) except with its zonal mean SST anomalies replaced by those from Fig. 9e (AM4-ESM2Mpattern2K-125). Figure 9l highlights the SST differences between AM4-CM4pattern2K-125 and AM4-CM4pattern2K-125-modified. See Table 2 for a detailed description of these simulations.

The spatial distribution of TOA net radiative feedback in response to the various SST warming patterns is shown in Fig. 10 with the global mean feedback shown on the top of each panel. The global mean feedback in AM4-CM4pattern2K-50 (-1.78 W m^{-2} K^{-1}) and AM4-CM4pattern2K-125 (-1.63 W m^{-2} K^{-1}) does not appear to differ substantially from AM4-uniform2K (-1.66 W m^{-2} K^{-1}), which seems to indicate that CM4.0's SST warming pattern does not contribute much to its increase in TOA feedback and EffCS compared to that inferred from the AM4.0 Cess simulation. However, Fig. 10c shows that the global mean feedback increases (less negative) by ~50% as CM4.0's SST warming pattern evolves from the earlier to the later period, which is also broadly consistent with Figs. 5c and 7c,f. This large increase (less negative) in global feedback strength in response to changes of SST warming pattern (AM4-CM4pattern2K-125minus50) indicates that AM4.0's global feedback is indeed sensitive to particular features of SST warming patterns and the relatively similar global feedback values between AM4-CM4pattern2K-50 (AM4-CM4pattern2K-125) and AM4-uniform2K may be due to the relatively small differences between these warming patterns and the uniform warming and global cancellation of regional changes in feedback instead of the model's lack of sensitivity to any SST warming patterns.

Indeed, Figs. 10d–f show that using ESM2M's SST warming patterns AM4.0 produces global feedbacks that are ~0.5 W m^{-2} K^{-1} smaller (more negative) than those produced by using CM4.0's warming patterns. This suggests that CM4.0's EffCS would be much lower if CM4.0 produced a similar SST warming pattern as ESM2M does. Figures 10g–i show that the additional positive feedback generated by CM4.0's warming patterns tends to be dominated by the SH oceans especially over the southeastern Pacific, the South Atlantic, and most of the Southern Ocean where CM4.0 produces the largest SST warming compared to ESM2M (see Figs. 9g–i). Figure 10k further shows that the

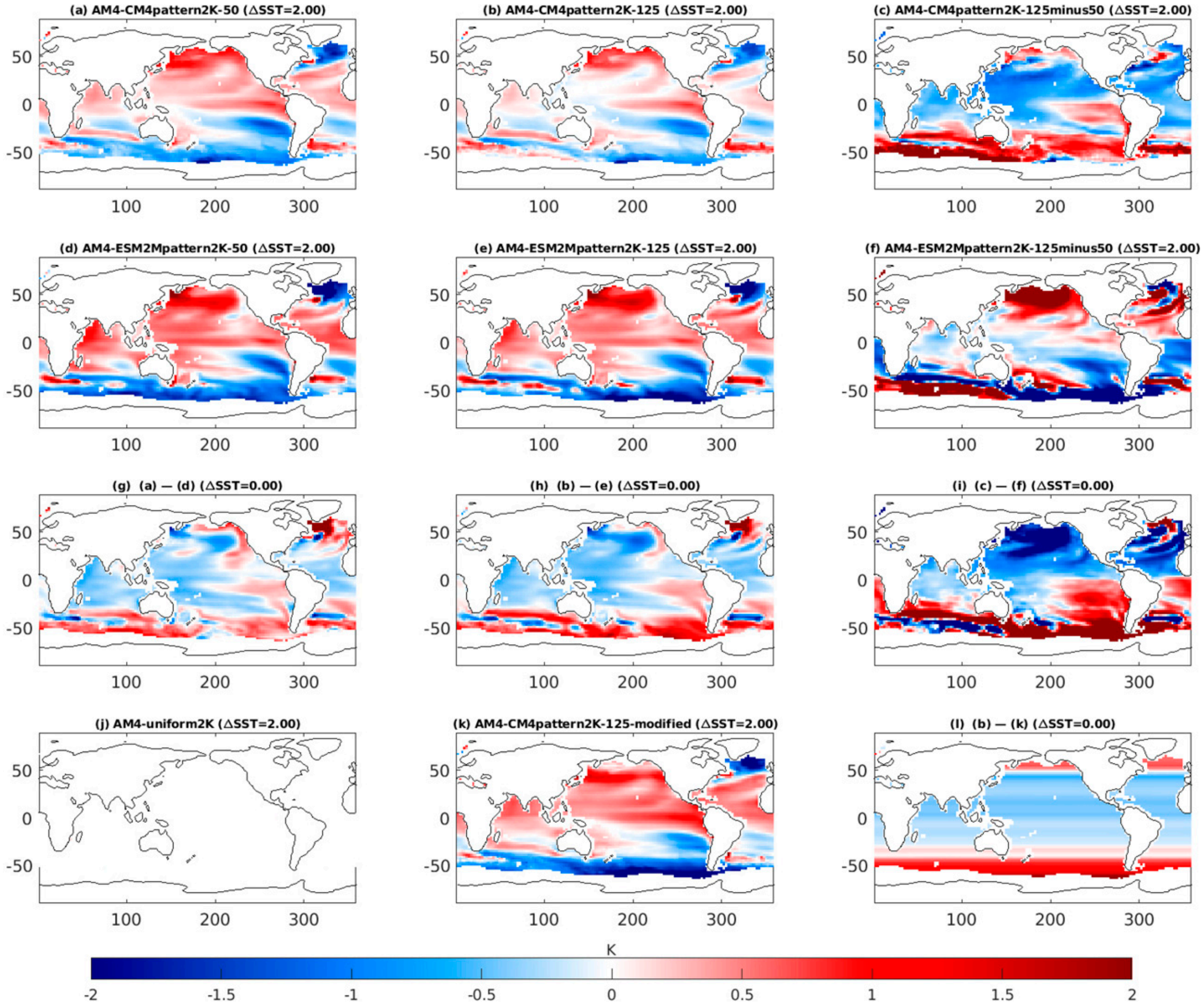

FIG. 9. Geographical distribution of the SST anomalies used for various SST warming pattern simulations (all use AM4-CM4-C as a control). The global ocean area-weighted mean SST anomaly is 2 K for all cases and is removed from each map. (a)–(c) SST anomalies derived from (a) years 26–75 (AM4-CM4pattern2K-50) and (b) years 101–150 (AM4-CM4pattern2K-125) of CM4.0's 4xCO_2 simulation and its pi-Control. (c) SST anomalies derived from the above two periods (AM4-CM4pattern2K-125minus50). (d)–(f) As in (a)–(c), but for SST anomalies derived from ESM2M's 4xCO_2 and pi-Control (i.e., AM4-ESM2Mpattern2K-50, AM4-ESM2Mpattern2K-125, and AM4-ESM2Mpattern2K-125minus50). (g)–(i) As in (a)–(c), but showing the difference in SST warming anomalies between CM4.0 and ESM2M. (j) Uniform 2-K SST warming (AM4-uniform2K). (k) As in (b), but with the zonal mean SST anomalies replaced by that from (e) (AM4-CM4pattern2K-125-modified). (l) The difference between (b) and (k). The global ocean area-weighted mean value is shown on the top of each panel. See Table 2 for a description of the simulations.

feedback increase from CM4.0's warming pattern results primarily from its zonal mean component because replacing its zonal mean SST anomalies with ESM2M's values leads to a large decrease (more negative) in global feedback. It brings down the global feedback from -1.63 W m^{-2} K^{-1} in AM4-CM4pattern2K-125 to -2.02 W m^{-2} K^{-1} in AM4-CM4pattern2K-125-modified, which is fairly close to -2.13 W m^{-2} K^{-1} in AM4-ESM2Mpattern2K-125. Comparing Figs. 10l and 10h confirms that the zonal mean difference in SST warming accounts for most of the feedback difference between AM4-CM4pattern2K-125 and AM4-ESM2Mpattern2K-125 including both spatial distribution and their global mean difference (78% = 0.39/0.5).

The differences in TOA net radiative feedback among the various SST warming pattern simulations result primarily from the model's differences in cloud feedback (see Fig. 11). For example, comparing Figs. 11a,c and Figs. 10a,c indicates that most of the increase (0.96 W m^{-2} K^{-1}) in global feedback from AM4-CM4pattern2K-50 (-1.78 W m^{-2} K^{-1}) to AM4-CM4pattern2K-125minus50 (-0.82 W m^{-2} K^{-1}) is due to an increase in cloud feedback (0.79 W m^{-2} K^{-1}). This suggests that changes in cloud feedback are the primary cause of feedback increase between the earlier and later periods of CM4.0's 4xCO_2 simulation. The same is true for SPEAR and SPEAR-SV (not shown). Similarly, most of the feedback

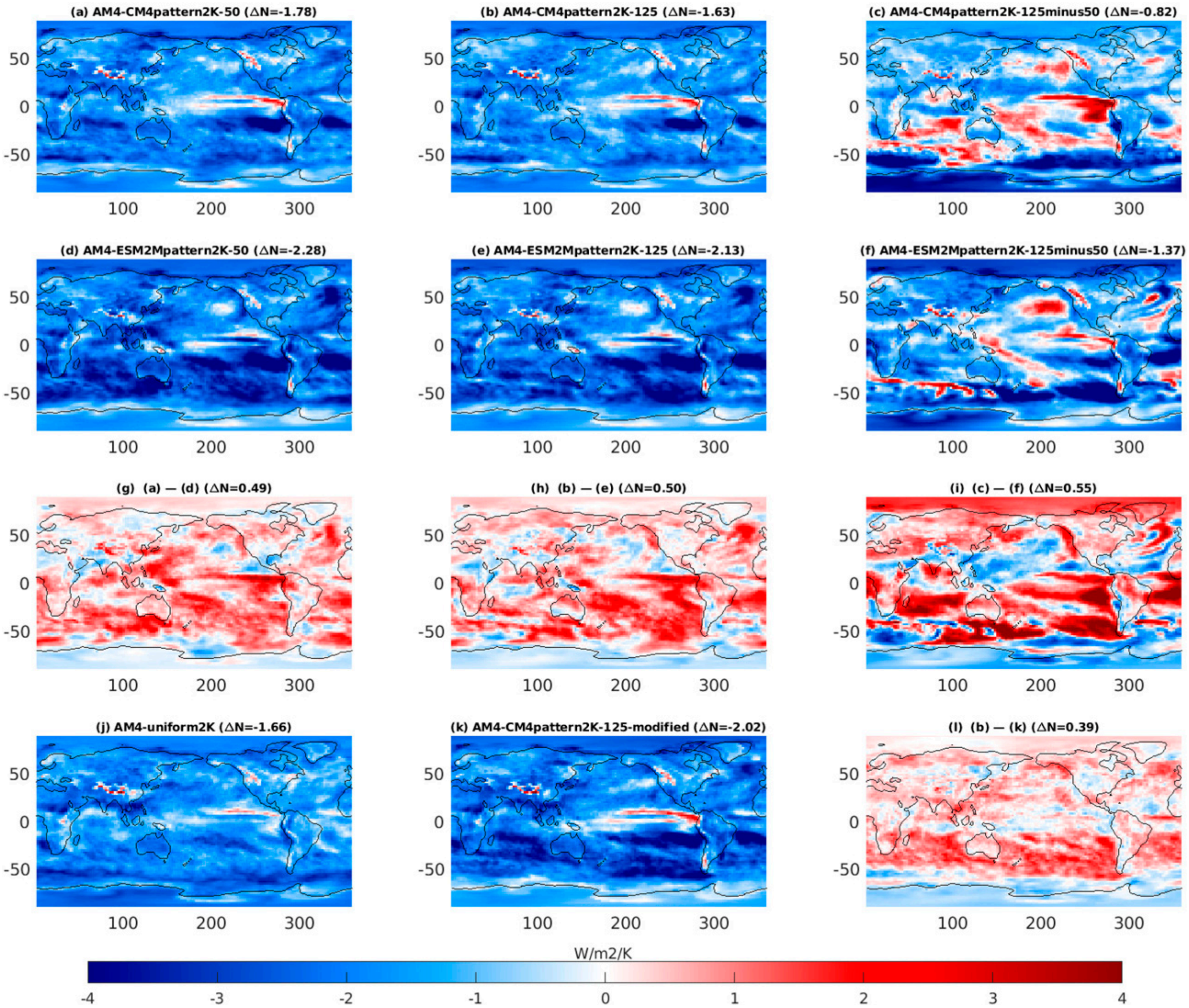

FIG. 10. As in Fig. 9, but for TOA net radiative feedback (W m^{-2} K^{-1}) computed from each SST warming pattern simulation and the control (AM4-CM4-C). See Table 2 for a description of the simulations.

increase from AM4-ESM2Mpattern2K-50 (-2.28 W m^{-2} K^{-1}) to AM4-ESM2Mpattern2K-125minus50 (-1.37 W m^{-2} K^{-1}) is also caused by their cloud feedback difference. Furthermore, Figs. 11g–i show very similar spatial patterns as well as magnitudes to Figs. 10g–i, indicating that it is the cloud feedback difference that dominates the total feedback difference produced by CM4.0's and ESM2M's SST warming patterns. By contrast, the clear-sky feedback (supplementary Figs. 4g–i) exhibits little similarity to Figs. 10g–i. Comparing Figs. 10g,h and Figs. 11g,h, and supplementary Figs. 4g and 4h suggests that roughly 80% (20%) of the global feedback difference between AM4-CM4pattern2K-50 and AM4-ESM2Mpattern2K-50 is due to cloud (clear-sky) feedback difference. The same is true for the difference between AM4-CM4pattern2K-125 and AM4-ESM2Mpattern2K-125. Moreover, the feedback difference between AM4-CM4pattern2K-125minus50 and AM4-ESM2Mpattern2K-125minus50 is almost entirely explained by their cloud feedback difference. Here, it is worth noting that the increase in global mean cloud feedback (0.4 W m^{-2} K^{-1}; Fig. 11h) resulting from the different SST warming patterns produced by CM4.0 and ESM2M is consistent with their difference in global mean cloud feedback in coupled simulations (0.42 W m^{-2} K^{-1}; Fig. 6b). Figure 6 has also shown that the cloud feedback difference between CM4.0 and ESM2M is the leading cause of CM4.0's increase in total feedback compared to ESM2M. Finally, Figs. 11h and 11l further demonstrate that the zonal mean difference in SST warming patterns between CM4.0 and ESM2M is the primary cause of their difference in cloud feedback.

The TOA net cloud feedback and its sensitivity to various SST warming patterns are dominated by the shortwave (SW) component. Figure 12 shows that both the spatial distribution and the global mean values of TOA net cloud feedback shown in Fig. 11 are broadly similar to its SW component with the longwave (LW) component exhibiting little similarity (not shown). Figure 13 further reveals that the SW cloud feedback sensitivity to SST warming patterns is due primarily to

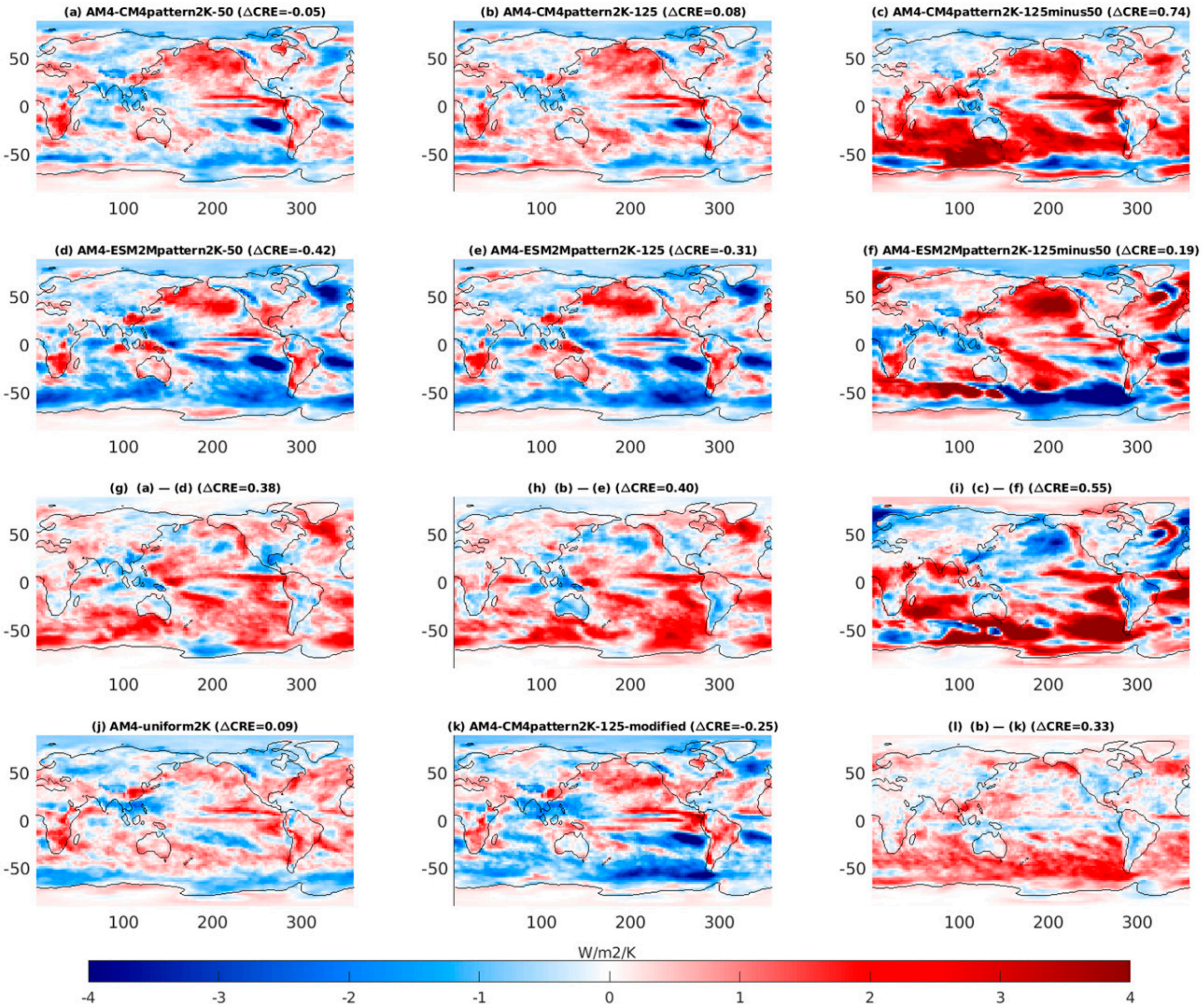

FIG. 11. As in Fig. 10, but for TOA net cloud feedback computed as changes in TOA net cloud radiative effect (ΔCRE) normalized to per 1 K global mean surface air temperature warming (W m^{-2} K^{-1}).

low cloud feedback sensitivity to SST warming patterns. In particular, Fig. 13 demonstrates that compared to ESM2M's SST warming pattern, CM4.0's relatively more SST warming over the eastern Pacific and Southern Ocean tends to reduce low cloud amount over the broad SH oceans, which decreases the reflection of SW radiation and therefore leads to more positive cloud feedback. Comparing Figs. 12h,l and Figs. 13h,l indicates again that the zonal mean difference between CM4.0's and ESM2M's SST warming patterns explains most of their difference in low cloud feedback.

4. Summary

It has been proven difficult to understand and narrow down the uncertainties in climate models' EffCS despite its paramount importance for accurate future climate prediction. This is due at least in part to EffCS's dependence on the details of physics parameterizations, especially those related to clouds. Cloud feedbacks have long been identified as the primary source of uncertainty in climate models' EffCS (e.g., Bony et al. 2004; Myers et al. 2021). Because of this, we have paid special attention to cloud feedbacks during the development of GFDL's AM4.0 (Zhao et al. 2018a,b) by frequently conducting an idealized Cess simulation and comparing its cloud feedbacks and Cess climate sensitivity with the earlier GFDL models. The goal is to monitor and use the Cess sensitivity in combination with the model's aerosol forcing to roughly assess its ability in simulating the observed historical warming trend. AM4.0 produces a global climate feedback and Cess sensitivity very similar to the earlier GFDL model AM2 in response to a uniform 2-K SST warming. Yet, CM4.0 produces a much larger EffCS (5 K) than ESM2M (2.9 K), which uses AM2 and produces one of the lowest EffCS values among CMIP5 models (Meehl et al. 2020). This sharp contrast indicates that other components of CM4.0 and their interactions with AM4.0 can dramatically alter the EffCS of the coupled system. By comparing CM4.0 with SPEAR and SPEAR-SV, which use an identical AM4.0 but a different ocean and sea ice

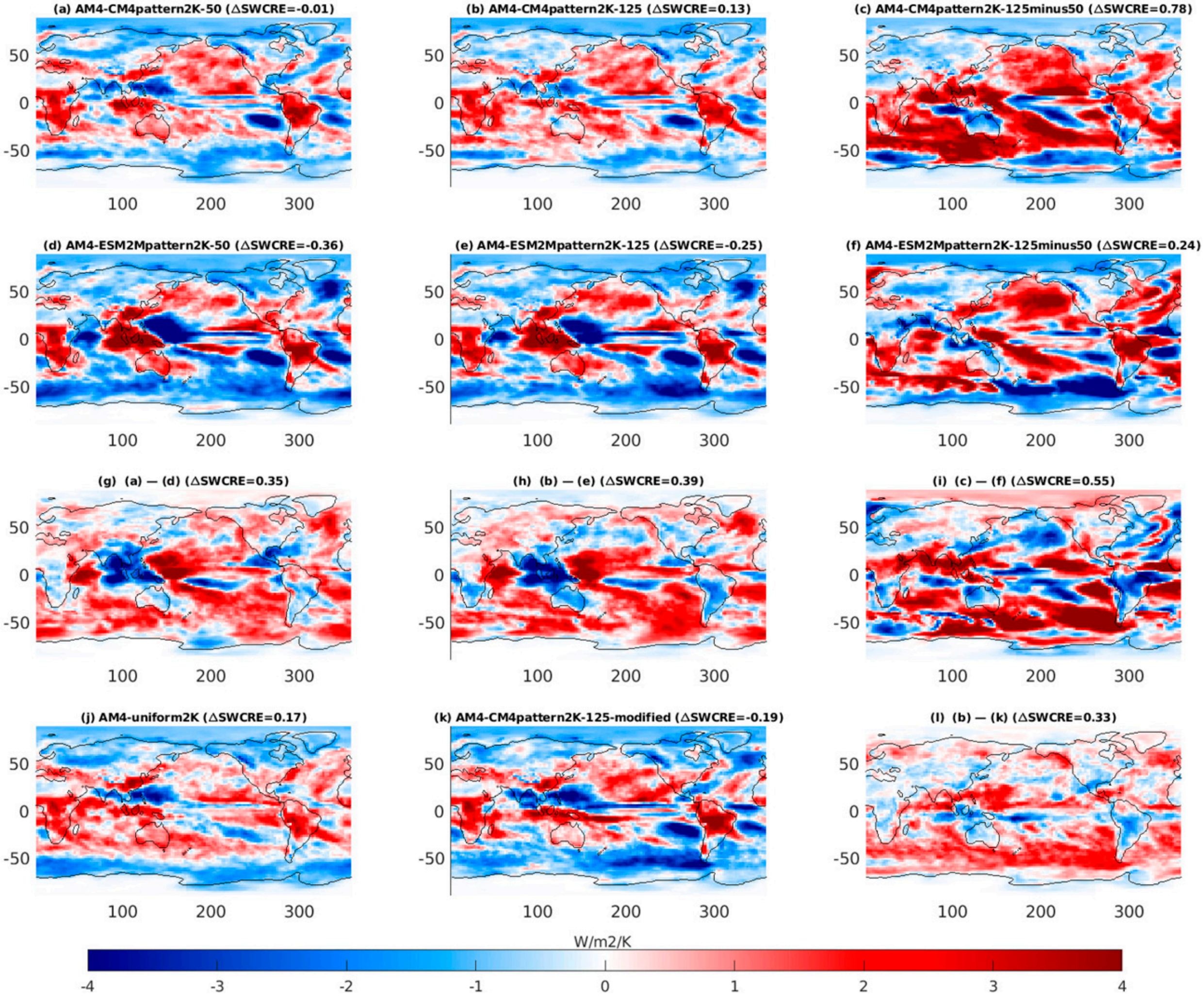

FIG. 12. As in Fig. 10, but for TOA SW cloud feedback computed as changes in TOA SW cloud radiative effect (ΔSWCRE) normalized to per 1 K global mean surface air temperature warming (W m^{-2} K^{-1}).

model with (SPEAR) or without (SPEAR-SV) the dynamical vegetation model, we find that CM4.0 produces an EffCS roughly 20% and 30% higher than SPEAR (EffCS = 4.2 K) and SPEAR-SV (EffCS = 3.8 K), respectively (Fig. 1b). The substantial increase in CM4.0's EffCS is found to be caused primarily by an additional positive forcing associated with the direct response of vegetation to CO_2 increase (Figs. 3 and 4) and an enhanced positive feedback due to its stronger reduction in SH SICs (Figs. 6d,e). While the temperature-mediated change in vegetation has substantial regional impact on feedback its contribution to the global mean feedback is relatively small (Figs. 5j,k and 7j,k).

Although cloud feedback does not explain the key feedback differences among CM4.0, SPEAR, and SPEAR-SV (Figs. 6a,b), it is the primary cause of the models' increase in TOA net feedback during the later period of their $4xCO_2$ simulations (supplementary Fig. 3). The increase in cloud feedback is caused by the change in SST warming patterns (Figs. 11a,c). Compared to the earlier period, all of the three models produce more relative warming over the eastern Pacific and the Southern Ocean. This change in SST warming patterns reduces low cloud amount (Figs. 13a,c) and increases downward SW radiation (Figs. 12a,c) over the broad SH oceans and the eastern Pacific, resulting in a substantial increase in global net feedback.

Compared to the GFDL's new climate models, ESM2M stands out by its much smaller (less positive or more negative) cloud feedback (Fig. 6b). In addition, ESM2M also exhibits a much smaller reduction in SH SICs (Fig. 6e) and therefore substantially weaker positive clear-sky SW feedback over the Antarctic sea ice region, especially compared to CM4.0 (Fig. 6d). Indeed, compared to ESM2M, CM4.0 produces a 0.86 W m^{-2} K^{-1} increase (less negative) in global mean feedback, among which 0.42 W m^{-2} K^{-1} is from cloud feedback and 0.23 W m^{-2} K^{-1} is from clear-sky SW feedback, with the rest being from clear-sky LW feedback (Figs. 6a–d). This indicates that cloud feedback is the leading cause of the increase in CM4.0's EffCS compared to ESM2M.

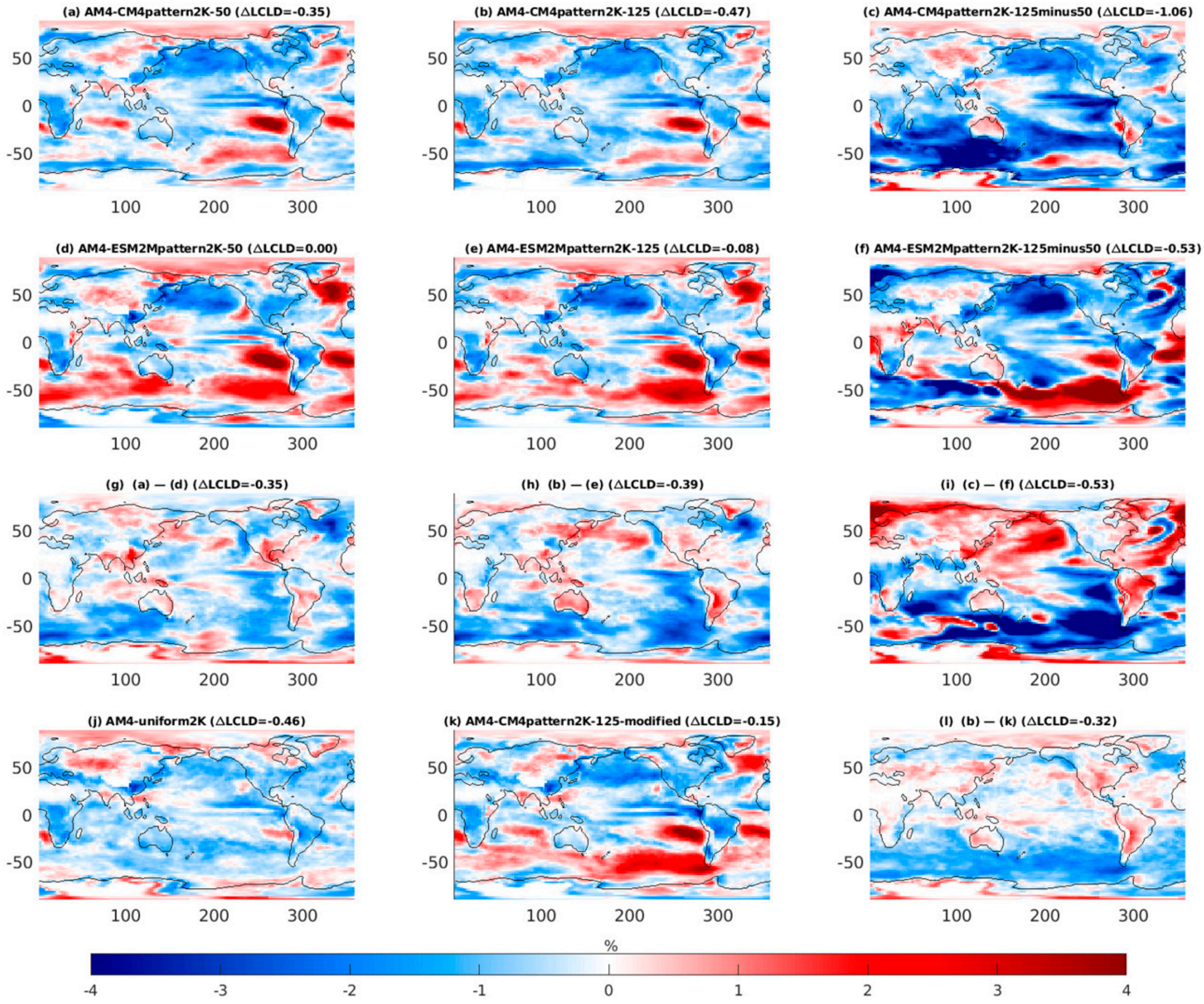

FIG. 13. As in Fig. 10, but for low cloud amount feedback computed as changes in low cloud amount (ΔLCLD) normalized to per 1 K global mean surface air temperature warming (% K^{-1}).

The cloud feedback difference between CM4.0 and ESM2M is due primarily to their difference in SST warming patterns. The uncoupled AM4.0 forced by CM4.0's SST warming pattern produces a global TOA feedback ~0.5 W m^{-2} K^{-1} higher than AM4.0 forced by ESM2M's SST warming pattern (Fig. 10h). Roughly 80% (0.4 W m^{-2} K^{-1}) of the increase is due to cloud feedback (Fig. 11h). This number is also consistent with the cloud feedback difference (0.42 W m^{-2} K^{-1}) computed directly from CM4.0 and ESM2M (Fig. 6b). The difference in cloud feedback results predominantly from low cloud cover and their associated SW feedback in response to the different SST warming patterns (Figs. 12 and 13). Compared to ESM2M, CM4.0 produces more relative warming over the eastern Pacific and the Southern Ocean, which tends to reduce low cloud cover and increase downward SW radiation over the eastern Pacific and much of the broader SH oceans. Further experiments demonstrate that it is the zonal mean difference in the SST warming patterns between CM4.0 and ESM2M that dominates their cloud feedback difference. Thus, the cloud feedback difference in response to CM4.0's and ESM2M's SST warming patterns appears to be the leading cause of CM4.0's increase in EffCS compared to ESM2M.

Despite AM4.0's large sensitivity of cloud feedback to SST warming patterns produced by CM4.0 and ESM2M, it is worth noting that the global mean cloud feedback derived from some of the CM4.0's SST warming patterns appears to be fairly well captured by the Cess uniform warming simulation (e.g., comparing panels b and j of Figs. 10–13). One interpretation might be that the Cess experiment remains a good predictor of the feedbacks over the first century or so, but cannot predict the longer-term SST pattern changes and the resulting feedback changes that affect the eventual EffCS (i.e., the two-part EffCS definition used in this paper). This is in general consistent with Qin et al. (2022), who suggest that the Cess experiment in conjunction with the ERF derived from an AMIP-4xCO_2 simulation can capture a large fraction (40%–60%) of CMIP models' variance in cloud feedback and the traditional EffCS defined by a single linear regression over the first 150 years of $4xCO_2$ simulation from a Gregory plot. However, it does not necessarily mean that SST warming patterns are unimportant for an individual model's cloud feedback at the earlier stage of its $4xCO_2$ simulations. The results from ESM2M's SST pattern provide an example of the importance of some features of SST warming patterns to AM4.0 no matter when they might take place. Indeed, the results of Qin et al. (2022) also reveal a substantial fraction of intermodel variation in cloud feedback and EffCS that cannot be explained by the Cess uniform warming simulations. Thus, this study offers a complementary viewpoint to fully account for intermodel differences in cloud feedback and climate sensitivity in coupled models.

Although the limitations of the Cess experiment have been pointed out in many previous studies (e.g., Ringer et al. 2014), we emphasize here the necessity of expanding the traditional uncoupled approach (including both the Cess experiment for studying feedbacks and the $4xCO_2$ perturbation experiment for studying the ERF of $4xCO_2$) to take into account processes (e.g., dynamic vegetation and changes in SIC and SST warming patterns) important in a coupled system for studying and understanding the EffCS of a coupled climate or Earth system model. In particular, a dynamic vegetation model can produce a sizable increase in ERF in response to $4xCO_2$, which may take decades to reach an equilibrium state in an uncoupled model with fixed SSTs and SICs. This can pose a challenge for traditional approaches, which ignore this effect and may produce erroneous estimates of the forcing and feedback. We have demonstrated that a set of uncoupled atmospheric simulations that include dynamic vegetation and changes in SICs and SST warming patterns can well reproduce the changes in TOA radiation and SAT in response to a quadrupling of CO_2 concentration in a coupled system, and therefore are useful to disentangle various forcing and feedback mechanisms. However, the number of components/processes that need be included in uncoupled atmospheric model simulations would depend on the complexity of the coupled system.

While this study demonstrates the importance of SST warming patterns and changes in SICs and vegetation in affecting CM4.0's EffCS, several questions remain to be investigated. In particular, what aspects of the model differences may have caused the different SST warming patterns between ESM2M and CM4.0 including CM4.0's more late-stage warming in the SH high latitudes and southern subtropical upwelling regions? There are many differences between the two models including the formulations of their oceanic and atmospheric physics and dynamics, as well as their horizontal resolutions (see Table 3). In principle, this question can be sorted out through a series of simulations with incremental changes made from ESM2M to CM4.0. However, they are difficult to do in practice because each change would essentially create a new coupled model and require additional retuning and a long pi-Control simulation before we can do a $4xCO_2$ simulation. All of these require substantial computational resources. Nevertheless, the similar SST warming pattern between CM4.0 and SPEAR (supplementary Fig. 1) indicates that ocean and sea ice model resolution alone is unlikely the cause of the different SST warming patterns between CM4.0 and ESM2M. Moreover, compared to SPEAR, CM4.0's greater loss of Antarctic sea ice concentration in response to $4xCO_2$ cannot be simply attributed to its increased ocean and sea ice model resolution because they also differ in the oceanic physics parameterizations. For example, SPEAR includes a mesoscale eddy parameterization and an extra horizontal viscosity at high-latitude oceans while CM4.0 does not. Both SPEAR and CM4.0 use the same submesoscale eddy parameterization, but they choose different parameter coefficients. Although these and other differences in the oceanic physics parameterizations are motivated by their different ocean model resolutions (Delworth et al. 2020), they are not equivalent. Finally, it is interesting to explore what physical and/or biophysical processes might have set the multidecadal time scale of vegetation adjustment in CM4.0. We will leave an investigation of these questions to future work.

Acknowledgments. I acknowledge the World Climate Research Programme, which, through its Working Group on Coupled Modelling, coordinated and promoted CMIP6. Support from NOAA OAR leadership for this project is acknowledged. I am grateful for helpful comments and suggestions from John Dunne, Michael Winton, and Michael A. Zhao. I also thank the GFDL model development team, modeling service group, and the leadership of NOAA/GFDL for their efforts and support in developing CM4 and SPEAR. I am also grateful for the anonymous reviewers whose comments and suggestions have improved the paper.

Data availability statement. The CM4.0 simulation data are available at https://esgf-node.llnl.gov/search/cmip6/. SPEAR simulation data are available at ftp://data1.gfdl.noaa.gov/users/Tom.Delworth/SPEAR_Documentation_paper/SPEAR. AM4 simulation data can be obtained by conducting AM4 simulations using AM4 model code following the procedure described in section 2 of this paper. AM4 model code is provided at http://data1.gfdl.noaa.gov/nomads/forms/am4.0/.

REFERENCES

Adcroft, A., and Coauthors, 2019: The GFDL global ocean and sea ice model OM4.0: Model description and simulation features. *J. Adv. Model. Earth Syst.*, **11**, 3167–3211, https://doi.org/10.1029/2019MS001726.

Anderson, J. L., and Coauthors, 2004: The new GFDL global atmosphere and land model AM2/LM2: Evaluation with prescribed SST simulations. *J. Climate*, **17**, 4641–4673, https://doi.org/10.1175/JCLI-3223.1.

Andrews, T., and M. J. Webb, 2018: The dependence of global cloud and lapse rate feedbacks on the spatial structure of tropical Pacific warming. *J. Climate*, **31**, 641–654, https://doi.org/10.1175/JCLI-D-17-0087.1.

——, J. M. Gregory, M. J. Webb, and K. E. Taylor, 2012: Forcing, feedbacks and climate sensitivity in CMIP5 coupled atmosphere–ocean climate models. *Geophys. Res. Let.*, **39**, L09712, https://doi.org/10.1029/2012GL051607.

——, ——, and ——, 2015: The dependence of radiative forcing and feedback on evolving patterns of surface temperature change in climate models. *J. Climate*, **28**, 1630–1648, https://doi.org/10.1175/JCLI-D-14-00545.1.

——, ——, D. Paynter, L. G. Silvers, C. Zhou, and T. Mauritsen, 2018: Accounting for changing temperature patterns increases historical estimates of climate sensitivity. *Geophys. Res. Lett.*, **45**, 8490–8499, https://doi.org/10.1029/2018GL078887.

Bony, S., and J.-L. Dufresne, 2005: Marine boundary layer clouds at the heart of tropical cloud feedback uncertainties in climate models. *Geophys. Res. Lett.*, **32**, L20806, https://doi.org/10.1029/2005GL023851.

——, ——, H. L. Treut, J.-J. Morcrette, and C. Senior, 2004: On dynamic and thermodynamic components of cloud changes. *Climate Dyn.*, **22**, 71–86, https://doi.org/10.1007/s00382-003-0369-6.

Bretherton, C. S., 2015: Insights into low-latitude cloud feedbacks from high-resolution models. *Philos. Trans. Roy. Soc.*, **A373**, 20140415, https://doi.org/10.1098/rsta.2014.0415.

Brient, F., and T. Schneider, 2016: Constraints on climate sensitivity from space-based measurements of low-cloud reflection. *J. Climate*, **29**, 5821–5835, https://doi.org/10.1175/JCLI-D-15-0897.1.

Cess, R., and Coauthors, 1990: Intercomparison and interpretation of climate feedback processes in 19 atmospheric general circulation models. *J. Geophys. Res.*, **95**, 16 601–16 615, https://doi.org/10.1029/JD095iD10p16601.

——, and Coauthors, 1996: Cloud feedback in atmospheric general circulation model: An update. *J. Geophys. Res.*, **101**, 12 791–12 794, https://doi.org/10.1029/96JD00822.

Cox, P. M., C. Huntingford, and M. S. Williamson, 2018: Emergent constraint on equilibrium climate sensitivity from global temperature variability. *Nature*, **553**, 319–322, https://doi.org/10.1038/nature25450.

Delworth, T. L., and Coauthors, 2020: SPEAR: The next generation GFDL modeling system for seasonal to multidecadal prediction and projection. *J. Adv. Model. Earth Syst.*, **12**, e2019MS001895, https://doi.org/10.1029/2019MS001895.

Dong, Y., C. Proistosescu, K. C. Armour, and D. S. Battisti, 2019: Attributing historical and future evolution of radiative feedbacks to regional warming patterns using a Green's function approach: The preeminence of the western Pacific. *J. Climate*, **32**, 5471–5491, https://doi.org/10.1175/JCLI-D-18-0843.1.

Dunne, J. P., J. G. John, A. J. Adcroft, S. M. Griffies, R. W. Hallberg, E. Shevliakova, and R. J. Stouffer, 2012: GFDL's ESM2 global coupled climate–carbon Earth system models. Part I: Physical formulation and baseline simulation characteristics. *J. Climate*, **25**, 6646–6665, https://doi.org/10.1175/JCLI-D-11-00560.1.

Eyring, V., S. Bony, G. Meehl, C. A. Senior, B. Stevens, R. Stouffer, and K. E. Taylor, 2016: Overview of the Coupled Model Intercomparison Project Phase 6 (CMIP6) experimental design and organization. *Geosci. Model Dev.*, **9**, 1937–1958, https://doi.org/10.5194/gmd-9-1937-2016.

Gregory, J. M., and T. Andrews, 2016: Variation in climate sensitivity and feedback parameters during the historical period. *Geophys. Res. Lett.*, **43**, 3911–3920, https://doi.org/10.1002/2016GL068406.

——, and Coauthors, 2004: A new method for diagnosing radiative forcing and climate sensitivity. *Geophys. Res. Lett.*, **31**, L03205, https://doi.org/10.1029/2003GL018747.

——, T. Andrews, P. Ceppi, T. Mauritsen, and M. J. Webb, 2020: How accurately can the climate sensitivity to CO_2 be estimated from historical climate change? *Climate Dyn.*, **54**, 129–157, https://doi.org/10.1007/s00382-019-04991-y.

Grose, M. R., J. Gregory, R. Colman, and T. Andrews, 2018: What climate sensitivity index is most useful for projections? *Geophys. Res. Lett.*, **45**, 1559–1566, https://doi.org/10.1002/2017GL075742.

Hansen, J., R. Ruedy, M. Sato, and K. Lo, 2005: Efficacy of climate forcings. *J. Geophys. Res.*, **110**, D18104, https://doi.org/10.1029/2005JD005776.

Held, I. M., and Coauthors, 2019: Structure and performance of GFDL's CM4.0 climate model. *J. Adv. Model. Earth Syst.*, **11**, 3691–3727, https://doi.org/10.1029/2019MS001829.

Klein, S. A., and A. Hall, 2015: Emergent constraints for cloud feedbacks. *Curr. Climate Change Rep.*, **1**, 276–287, https://doi.org/10.1007/s40641-015-0027-1.

Medeiros, B., B. Stevens, I. M. Held, M. Zhao, D. L. Williamson, J. Olson, and C. S. Bretherton, 2008: Aquaplanets, climate sensitivity, and low clouds. *J. Climate*, **21**, 4974–4991, https://doi.org/10.1175/2008JCLI1995.1.

Meehl, G. A., C. A. Senior, V. Eyring, G. Flato, J.-F. Lamarque, R. J. Stouffer, K. E. Taylor, and M. Schlund, 2020: Context for interpreting equilibrium climate sensitivity and transient climate response from the CMIP6 Earth system models. *Sci. Adv.*, **6**, eaba1981, https://doi.org/10.1126/sciadv.aba1981.

Myers, T. A., R. C. Scott, M. D. Zelinka, S. A. Klein, J. R. Norris, and P. M. Caldwell, 2021: Observational constraints on low cloud feedback reduce uncertainty of climate sensitivity. *Nat. Climate Change*, **11**, 501–507, https://doi.org/10.1038/s41558-021-01039-0.

Paynter, D. J., and T. L. Frölicher, 2015: Sensitivity of radiative forcing, ocean heat uptake, and climate feedback to changes in anthropogenic greenhouse gases and aerosols. *J. Geophys. Res. Atmos.*, **120**, 9837–9854, https://doi.org/10.1002/2015JD023364.

Qin, Y., M. D. Zelinka, and S. A. Klein, 2022: On the correspondence between atmosphere-only and coupled simulations for radiative feedbacks and forcing from CO_2. *J. Geophys. Res. Atmos.*, **127**, e2021JD035460, https://doi.org/10.1029/2021JD035460.

Ringer, M. A., T. Andrews, and M. J. Webb, 2014: Global-mean radiative feedbacks and forcing in atmosphere-only and coupled atmosphere–ocean climate change experiments. *Geophys. Res. Lett.*, **41**, 4035–4042, https://doi.org/10.1002/2014GL060347.

Rugenstein, M. A. A., and K. C. Armour, 2021: Three flavors of radiative feedbacks and their implications for estimating equilibrium climate sensitivity. *Geophys. Res. Lett.*, **48**, e2021GL092983, https://doi.org/10.1029/2021GL092983.

Satoh, M., and Coauthors, 2018: Toward reduction of the uncertainties in climate sensitivity due to cloud processes using a global non-hydrostatic atmospheric model. *Prog. Earth Planet. Sci.*, **5**, 67, https://doi.org/10.1186/s40645-018-0226-1.

Schlund, M., A. Lauer, P. Gentine, S. C. Sherwood, and V. Eyring, 2020: Emergent constraints on equilibrium climate sensitivity in CMIP5: Do they hold for CMIP6? *Earth Syst. Dyn.*, **11**, 1233–1258, https://doi.org/10.5194/esd-11-1233-2020.

Sherwood, S., S. Bony, and J.-L. Dufresne, 2014: Spread in model climate sensitivity traced to atmospheric convective mixing. *Nature*, **505**, 37–42, https://doi.org/10.1038/nature12829.

——, and Coauthors, 2020: An assessment of Earth's climate sensitivity using multiple lines of evidence. *Rev. Geophys.*, **58**, e2019RG000678, https://doi.org/10.1029/2019RG000678.

Shevliakova, E., and Coauthors, 2009: Carbon cycling under 300 years of land use change: Importance of the secondary vegetation sink. *Global Biogeochem. Cycles*, **23**, GB2022, https://doi.org/10.1029/2007GB003176.

Silvers, L. G., D. J. Paynter, and M. Zhao, 2018: The diversity of cloud responses to twentieth century sea surface temperatures. *Geophys. Res. Lett.*, **45**, 391–400, https://doi.org/10.1002/2017GL075583.

Soden, B., A. Broccoli, and R. Hemler, 2004: On the use of cloud forcing to estimate cloud feedback. *J. Climate*, **17**, 3661–3665, https://doi.org/10.1175/1520-0442(2004)017<3661:OTUOCF>2.0.CO;2.

Webb, M. J., and Coauthors, 2006: On the contribution of local feedback mechanisms to the range of climate sensitivity in two GCM ensembles. *Climate Dyn.*, **27**, 17–38, https://doi.org/10.1007/s00382-006-0111-2.

——, F. H. Lambert, and J. Gregory, 2013: Origins of differences in climate sensitivity, forcing and feedback in climate models. *Climate Dyn.*, **40**, 677–707, https://doi.org/10.1007/s00382-012-1336-x.

——, and Coauthors, 2015: The impact of parametrized convection on cloud feedback. *Philos. Trans. Roy. Soc.*, **A373**, 20140414, https://doi.org/10.1098/rsta.2014.0414.

Wing, A. A., and Coauthors, 2020: Clouds and convective self-aggregation in a multimodel ensemble of radiative–convective-equilibrium simulations. *J. Adv. Model. Earth Syst.*, **12**, e2020MS002138, https://doi.org/10.1029/2020MS002138.

Winton, M., K. Takahashi, and I. M. Held, 2010: Importance of ocean heat uptake efficacy to transient climate change. *J. Climate*, **23**, 2333–2344, https://doi.org/10.1175/2009JCLI3139.1.

——, and Coauthors, 2019: Climate sensitivity of GFDL's CM4.0. *J. Adv. Model. Earth Syst.*, **12**, e2019MS001838, https://doi.org/10.1029/2019MS001838.

Wyant, M. C., C. S. Bretherton, J. T. Bacmeister, J. T. Kiehl, I. M. Held, M. Zhao, S. A. Klein, and B. J. Soden, 2006: A comparison of low-latitude cloud properties and their response to climate change in three AGCMs sorted into regimes using mid-tropospheric vertical velocity. *Climate Dyn.*, **27**, 261–279, https://doi.org/10.1007/s00382-006-0138-4.

Zhang, M., and Coauthors, 2013: CGILS: Results from the first phase of an international project to understand the physical mechanisms of low cloud feedbacks in single column models. *J. Adv. Model. Earth Syst.*, **5**, 826–842, https://doi.org/10.1002/2013MS000246.

Zhao, M., 2014: An investigation of the connections among convection, clouds, and climate sensitivity in a global climate model. *J. Climate*, **27**, 1845–1862, https://doi.org/10.1175/JCLI-D-13-00145.1.

——, and Coauthors, 2016: Uncertainty in model climate sensitivity traced to representations of cumulus precipitation microphysics. *J. Climate*, **29**, 543–560, https://doi.org/10.1175/JCLI-D-15-0191.1.

——, and Coauthors, 2018a: The GFDL global atmosphere and land model AM4.0/LM4.0: 1: Simulation characteristics with prescribed SSTs. *J. Adv. Model. Earth Syst.*, **10**, 691–734, https://doi.org/10.1002/2017MS001208.

——, and Coauthors, 2018b: The GFDL global atmosphere and land model AM4.0/LM4.0: 2: Model description, sensitivity studies, and tuning strategies. *J. Adv. Model. Earth Syst.*, **10**, 735–769, https://doi.org/10.1002/2017MS001209.

Zhou, C., M. D. Zelinka, and S. A. Klein, 2017: Analyzing the dependence of global cloud feedback on the spatial pattern of sea surface temperature change with a Green's function approach. *J. Adv. Model. Earth Syst.*, **9**, 2174–2189, https://doi.org/10.1002/2017MS001096.